Development of a Light Force Accelerometer

by

David LaGrange Butts

B.A, Williams College (2006)

Submitted to the Department of Aeronautics and Astronautics
in partial fulfillment of the requirements for the degree of

Master of Science in Aeronautics and Astronautics

at the

MASSACHUSETTS INSTITUTE OF TECHNOLOGY

May 2008

Author .....
Department of Aeronautics and Astronautics
May 23, 2008

Certified by .....
Richard Stoner, Ph.D.
Principal Member of the Technical Staff
Thesis Supervisor

Certified by .....
Shaoul Ezekiel, Sc.D.
Professor of Aeronautics and Astronautics and
Electrical Engineering and Computer Science
Thesis Supervisor

Accepted by .....
David L. Darmofal
Associate Department Head
Chair, Committee on Graduate Students

Development of a Light Force Accelerometer

by

David LaGrange Butts

Submitted to the Department of Aeronautics and Astronautics
on May 23, 2008, in partial fulfillment of the
requirements for the degree of
Master of Science in Aeronautics and Astronautics

Abstract

In this work, the feasibility of a light force accelerometer was experimentally demonstrated. The light force accelerometer is an optical inertial sensor which uses focused laser light to levitate and trap glass microspheres as proof masses. Acceleration is measured by force rebalancing, which is exerted by radiation pressure from two counter-propagating laser beams. Proof mass displacements are measured by focusing light scattered by the proof mass on a position-sensitive photodetector. A simple model including laser relative intensity noise and shot noise from the measurement of the trapping beam powers estimates that the light force accelerometer could be capable of achieving a sensitivity of < 100 n$g/\text{Hz}^{1/2}$.

Essential components of this optical accelerometer, including the levitation of 10 μm glass microspheres in high vacuum and optical force rebalancing, were demonstrated with a single laser beam levitating a microsphere against gravity. Levitated particles are unstable in vacuum because of low viscous forces, so feedback stabilization is necessary for long term trapping. Preliminary performance diagnostics tested the short term sensitivity and bias stability of the apparatus for a constant 1 g acceleration. The factors currently limiting these performance parameters were determined to be bias instabilities associated with measurement of proof mass position and long term biases due to pressure-dependent radiometric effects.

Proposed modifications to the current apparatus include the implementation of a two-beam light force accelerometer and a more precise particle position detection method which is less sensitive to proof mass irregularities. This two-beam configuration enables operation in any orientation and permits complete characterization of accelerometer performance. Steps to develop a compact light force sensor in the future are also suggested.

Thesis Supervisor: Richard Stoner, Ph.D.
Title: Principal Member of the Technical Staff

Thesis Supervisor: Shaoul Ezekiel, Sc.D.
Title: Professor of Aeronautics and Astronautics and
Electrical Engineering and Computer Science

Acknowledgments

I have been fortunate to spend the last two years working with some remarkably smart and talented people who have supported my work at MIT. I would like to thank Dr. Richard Stoner and Dr. Brian Timmons for their dedicated support, mentoring, and friendship. Rick's grasp of physics, sense of humor, and professionalism are something to aspire to, and it was a pleasure working together. Brian's generosity and supportive understanding of graduate school's trials added much needed levity to the demands of grad student life. I am also indebted to his knowledge of lab hardware and software, which saved me countless hours of frustration and contributed to much of the progress I made in this project. It was a blast to work in a lab with a great crew— Paul Jones, J.P. Laine, Jason Langseth, Jesse Tawney, and many others. I would also like to thank the Draper Laboratory for supporting my fellowship, providing me with challenging research, and surrounding me with high caliber people.

I would like to thank Prof. Shaoul Ezekiel for his valuable guidance in developing this work, and for making it fun to talk about experiments. I would like to acknowledge Prof. Jeffrey Hoffman for helping me make the most of my time at MIT and making the transition to engineering a smooth one.

To my friends at MIT- Robert Panish, Matt Abrahamson, Russell Sargent, Chris Mandy, Bobby Legge, and many others- it's hard to imagine being at MIT without all of you.

I am grateful for my loving parents and sister who have encouraged me to excel in everything I do. I am also thankful for the love and support of my fiance, Erika Latham, and to have spent many great weekends away from Cambridge with her family in Westhampton, MA. Finally, I would like to recognize my grandfather, Frank Regensburg, who passed away during my first year at MIT. His encouragement and passionate interest in my endeavors helped me get to where I am today.

This thesis was prepared at the Charles Stark Draper Laboratory, Inc., under the Precise Inertial Sensing Internal Research and Development Contract CON05001-2 Project ID 21806 Activity ID 001.

Publication of this thesis does not constitute approval by Draper or the sponsoring agency of the findings or conclusions contained herein. It is published for the exchange and stimulation of ideas.

_____ _____

David Butts

Assignment

Draper Laboratory Report Number T-1609.

In consideration for the research opportunity and permission to prepare my thesis by and at The Charles Stark Draper Laboratory, Inc., I hereby assign my copyright of the thesis to The Charles Stark Draper Laboratory, Inc., Cambridge, Massachusetts.

5/22/08

David Butts Date

THIS PAGE INTENTIONALLY LEFT BLANK

Contents

THIS PAGE INTENTIONALLY LEFT BLANK

List of Figures

List of Tables

THIS PAGE INTENTIONALLY LEFT BLANK

Chapter 1

Introduction

1.1 Inertial navigation

Inertial navigation is a precise, instrumented method of 'dead reckoning,' in which acceleration in inertial space is sensed as an applied force on a physical body, and used to calculate the current position and velocity, or state. With a well-known initial state, the effects of these external forces on the body's motion may be continuously evolved without making external references to the vehicle's position, thus providing an 'onboard' method for navigation.

Inertial navigation systems, therefore, provide a determination of vehicle position and velocity in a chosen inertial reference frame without the need for external measurements, which all other navigation methods require. A system of onboard sensors and data processors perform navigation functions continuously by incorporating force measurements into models of vehicle dynamics and producing an estimate of current position and velocity. Given estimates of the initial state and subsequent measurements of acceleration and orientation, kinematic equations describing the motion of a body in inertial space may be integrated to compute the current state. Independent, onboard operation with automated computational tasks is the essential advantage of inertial navigation systems, since external measurements needed for other navigation systems may be intermittent, compromised, or inaccessible.

To determine position and velocity, an inertial navigation system must perform three functions. First, it must be able to refer inertial measurements to an inertial reference frame. This involves both a mechanization of inertial coordinates (e.g., geocentric longitude,

latitude, and altitude) relative to a body's physical coordinates (e.g., an aircraft's body axes shown in figure 1-2) and a computational relation between the body axes and other relevant coordinate frames. For instance, a satellite's body coordinates must be related to geocentric coordinates for navigation in orbit. The second function an inertial navigation

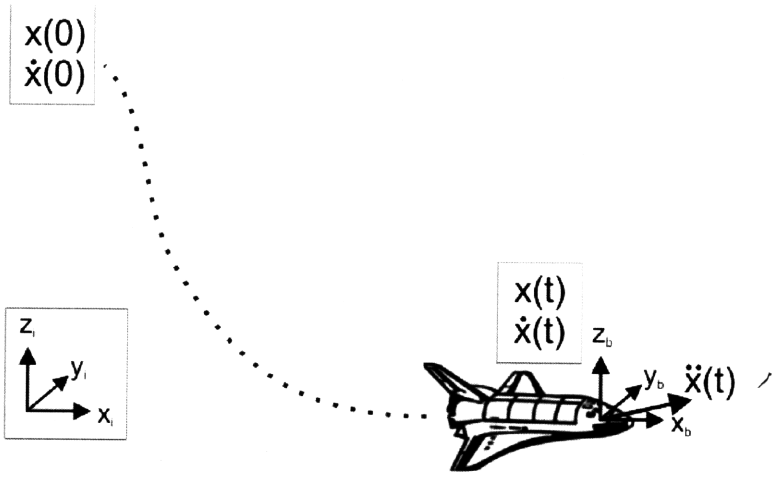

Figure 1-1: Principle of deduced, or 'dead' reckoning. If the original state $[\vec{x}(0), \dot{\vec{x}}(0)]$ is known and the system's orientation and acceleration over time are known, the state at time t can be completely reconstructed.

system performs is the measurement of specific force, or the change of a body's momentum relative to inertial space[1]. This is accomplished with accelerometers, sensors which measure specific force along sensitive axes. As shown in figure 1-2, an ensemble of three orthogonally-oriented accelerometers is implemented to measure inertial acceleration in all three dimensions. These accelerometers may be installed on a gyroscopically stabilized platform so that the accelerometers' axes are fixed relative to inertial space (platform system), or 'strapped' down to the body frame (strapdown system). In the latter case gyroscopes, which measure angular velocity, sense changes in body heading relative to inertial coordinates. A complete system of accelerometers and gyroscopes, as shown in figure 1-2, is called an inertial measurement unit (IMU).

The final function of an inertial navigation system is the integration of specific force measurements from accelerometers to determine velocity and position. Figure 1-3 shows a diagram of this computation. Numerically integrating Newton's kinematic equations in

[1]Specific force is measured as the difference between the body's acceleration in inertial space and the local gravitational force. Accelerometers measure specific force, not inertial acceleration.

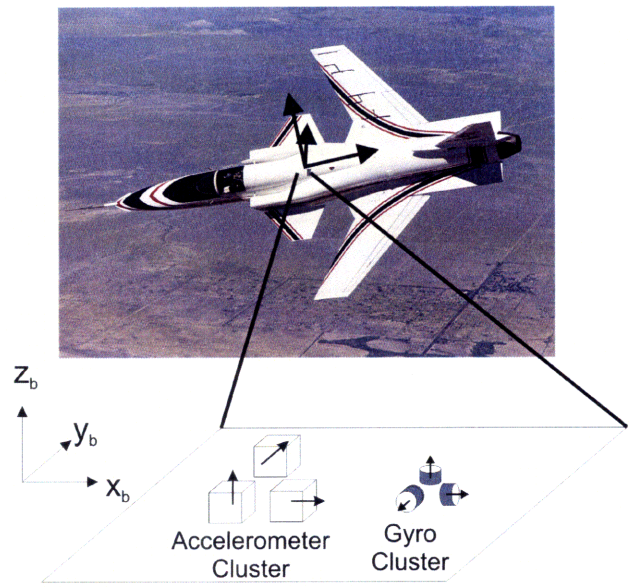

Figure 1-2: A complete inertial measurement unit (IMU) includes a cluster of three mutually orthogonal accelerometers and three gyroscopes. The body axes of the aircraft are indicated by x_b, y_b, and z_b.

three dimensions provides estimates of velocity and position. It should be noted that, due to the equivalence principle, it is impossible to distinguish gravitational forces from inertial accelerations (e.g., rocket thrust or vibrations) with accelerometer measurements alone. Models of local gravitational fields are required to calculate the gravitational component of the measured force. The equation to calculate inertial acceleration, $\ddot{\hat{\mathbf{r}}}^i$, from accelerometer measurements is:

$$\ddot{\hat{\mathbf{r}}}^i = \hat{\mathbf{C}}_a^i \tilde{\mathbf{f}}^a + \hat{\mathbf{G}}^i \tag{1.1}$$

where $\tilde{\mathbf{f}}^a$ is the specific force vector along accelerometer axes, $\hat{\mathbf{C}}_a^i$ is a rotational transformation from accelerometer axes to inertial coordinates, and $\hat{\mathbf{G}}^i$ is the computed acceleration due to gravity.

High precision sensors are essential for inertial navigation systems, since errors in accelerometer measurements lead to position errors which grow as the square of time (the result of integrating these measurements twice with respect to time). For instance, a constant accelerometer bias δa, or measured offset from the true acceleration, contributes to a

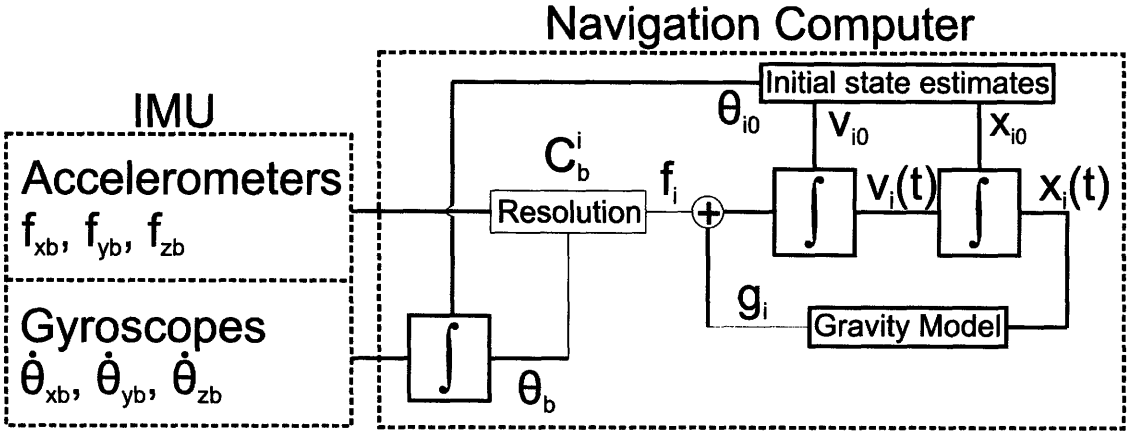

Figure 1-3: The computational function of an inertial navigation system integrates IMU measurements (f_i) and estimates local gravitational forces (g_i) to compute an estimate of the current position and velocity ($x_i(t)$ and $v_i(t)$).

position error δr in one dimension of

$$\delta r = v_0 t + \frac{1}{2}(\delta a)t^2 \tag{1.2}$$

where v_0 is the initial velocity. Therefore, a bias of 0.1 mg measured over one hour results in a position error of over 6 km (with $v_0 = 0$). While external measurements like radar position updates can reduce the growth of these errors, systems operating in environments without access to these references (e.g., long duration space flight) must rely on inertial navigation for long periods of time. These applications place a premium on the precision of inertial sensors.

1.1.1 History and applications

While gyroscopic measurements of the Earth's rotation were made as early as the 1850s, navigation applications of inertial sensing were not pursued until shortly before World War II, when German rocketry pioneers developed the V-2 with a complete gyro-stabilized IMU for trajectory control [Mac90], [Bar01]. In fact, guided missile and rocketry programs such as the U.S. Navy's Fleet Ballistic Missile program are responsible for driving much of the innovation in inertial guidance systems, both in improving the performance of inertial sensors and in revolutionizing the power and size of computers [Mac90].

In the 1960s, Charles Stark Draper headed the development of an IMU at the MIT Instrumentation Laboratory for spacecraft guidance and navigation as part of NASA's Apollo Program. Each flight to the Moon demonstrated that an inertial navigation system with updates from astronaut star-sightings (which soon became automated with star tracking cameras) could provide sufficient navigation accuracy for three-day spaceflights. Since the Apollo era, deep space missions such as the twin Voyager probes have used continuously operating inertial navigation systems for over thirty years. Similarly, submarines require high performance inertial navigation systems for underwater navigation over periods as long as several months.

Now that the need for precise inertial instruments has been motivated, a brief introduction to the principles of accelerometers is in order[2]. These concepts will help frame the discussion of the accelerometer which is the subject of this thesis.

1.2 Principles of accelerometers

Accelerometers measure the inertial force on a mass when it accelerates with respect to inertial space. A simple accelerometer, shown in figure 1-4 , includes a mass called the 'proof mass' which is connected to a case or platform by springs. If a force F is applied to the case, the proof mass will resist the force against the springs because of its inertia. As a result, the mass will be deflected with respect to the case. This displacement is proportionally related to the force applied to the case, so measurement of the proof mass displacement (made by a 'pick-off' device) provides a measure of F.

In the presence of gravitational forces, however, the case and proof mass accelerate together. Accelerometers are therefore not sensitive to gravitational acceleration. This fact is the underlying reason for requiring gravity models in inertial navigation systems to navigate in the presence of a gravitational field. An accelerometer measures specific force, or the non-gravitational force per unit mass.

[2]As gyroscopes are not the subject of this thesis, the fundamentals of their operation are not described here. Comprehensive descriptions of gyroscopic measurement and currently used gyroscopes can be found in [Law98] and [TiW04].

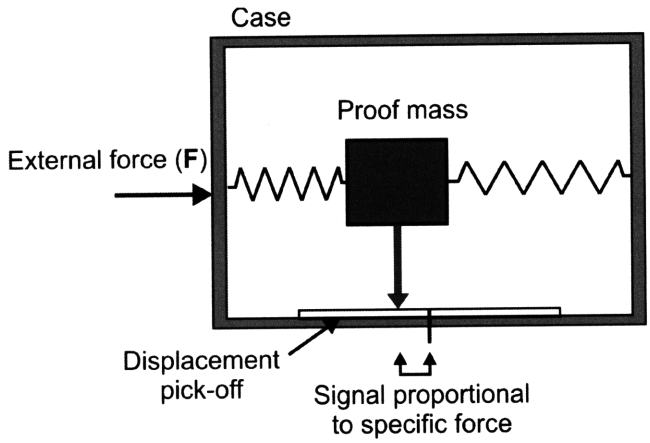

Figure 1-4: A simple mechanical accelerometer.

1.2.1 Force feedback accelerometers

The simple instrument shown in figure 1-4 may be described as an 'open loop' accelerometer, in that the measurement of specific force is made by passively tracking the deflections of the proof mass. An alternative approach to measuring specific force involves the use of actuators to 'null' or cancel proof mass motion from a 'zero' position, or set point. Figure 1-5 shows a basic force feedback accelerometer in which the deflections of a magnetic proof mass from the set point are nulled by electromagnetic forcers (magnetic coils). These forcers are controlled by a feedback controller known as a force rebalancing loop. The measurement of specific force is then made by monitoring the current applied to the forcers for rebalancing, as opposed to the measurement of proof mass motion.

Force feedback accelerometers are typically more precise because it is in general easier to measure a set point than a range of displacements. For systems measuring high acceleration, open loop accelerometers are typically limited by nonlinearities in the displacement per unit force (e.g., when spring extension is no longer linear). As a result, most high precision or high input accelerometers use force feedback.

1.3 Current accelerometers

Accelerometers are used in inertial navigation systems, as already discussed, but they serve a host of other applications as well. Some of these applications include equipment stabilization

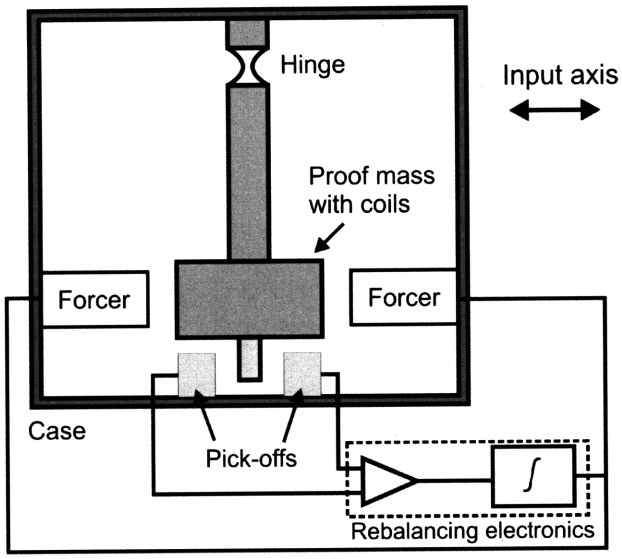

Figure 1-5: A force feedback pendulous accelerometer.

and control (e.g., active automobile suspension), gravimetry, and even entertainment (e.g., the Nintendo Wii controller). These applications demand a broad range of performance, size and cost requirements, and have influenced the development of several different classes of accelerometers. Mechanical accelerometers still achieve the highest performance overall, but microelectromechanical systems (MEMS) sensors are gaining prominence for their lower cost, batch manufacturability, low power usage, and reasonable performance (see figure 1-6). Table 1.3 summarizes typical performance parameters for several current sensors types.

The most commonly reported parameters are bias stability, scale factor stability, and resolution or sensitivity. Bias is a nonzero offset measured for zero acceleration input, and can change over time (hence, bias stability). Scale factor is the ratio of accelerometer output (e.g., an electrical current) to acceleration input. Scale factor can also change over time (hence, scale factor stability), leading to errors whenever there is a nonzero acceleration. Typically, the fractional variation over time is quoted in units of parts per million (ppm). Finally, resolution and sensitivity measure the lower limit in input below which acceleration measurement is masked by noise (usually quoted in g for resolution or $g/\mathrm{Hz}^{1/2}$ for sensitivity, since the measurement error due to white noise should decrease as the square root of the measurement interval).

Accelerometer Type	Mech. pendulous	MEMS pendulous	Silicon oscillating
Maximum input (g)	100	50	120
Scale factor stability (ppm)	100	500	5
Bias stability (μg)	0.1-10	100-1000	5
Resolution (μg)	10	1000	10

Table 1.1: Performance characteristics of several accelerometer types. The silicon oscillating accelerometer is one of the highest performance MEMS accelerometers to date. [TiW04], [BaS01]

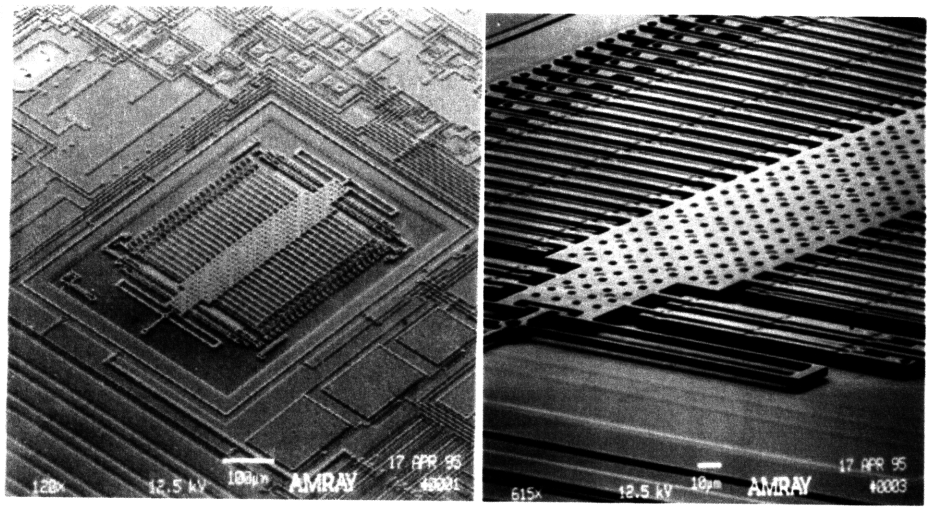

Figure 1-6: A MEMS accelerometer (left) with a close-up of its structure (right). [Analog Devices, Inc.]

1.3.1 Optical accelerometers

Rapid advances in commercially available compact laser systems, fiber optics, and electro-optic components have generated interest in developing high precision optical inertial sensors. Optical gyroscopes, such as the ring laser gyroscope and fiber optic gyroscope, are already being used for high-accuracy inertial navigation. Fewer optical accelerometers have been developed, but this class of sensors promises high performance, particularly in sensitivity and resolution. The fiber optic accelerometer, which measures phase shifts in an interferometer due to deflections of an optical fiber, has achieved a resolution of 1 μg [Tve80]. More recent optical accelerometer concepts, such as a microsphere optical resonator accelerometer (shown in figure 1-7) and the light force accelerometer presented in this thesis, may ultimately achieve sensitivities in the range of $ng/\mathrm{Hz}^{1/2}$ in simple, compact systems.

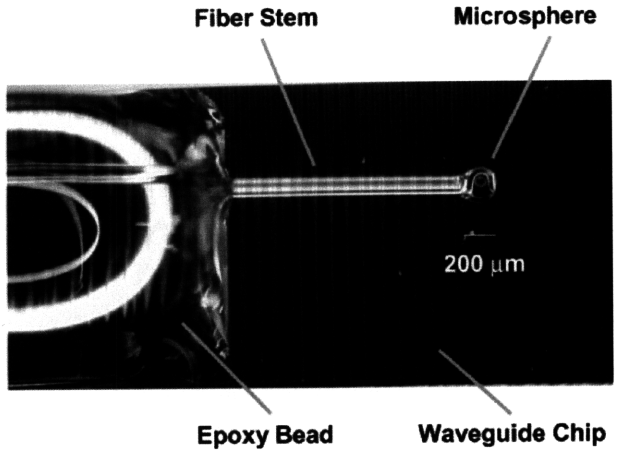

Figure 1-7: A microsphere fixed on the end of a fiber stem in a demonstration of a microsphere optical resonator accelerometer. Measurement of microsphere deflections via coupled light into a waveguide may provide μg resolution. [Lai01]

The light force accelerometer studied in this thesis is essentially an optical force rebalancing accelerometer; instead of using magnets to rebalance proof mass motion, it uses radiation pressure, or the momentum transfer from light to a reflecting object, provided by high power laser beams. The proof mass is a glass microsphere, which is levitated and trapped by two laser beams. In fact, the measurement of proof mass displacement and acceleration are both made by optical detection, allowing for high precision. This thesis takes a first step in demonstrating this interesting concept.

1.4 Overview of Thesis

This thesis covers the development of the light force accelerometer (LFA) concept to an experimental demonstration of the concept's major components, including laser levitation of glass microspheres in high vacuum and optical force rebalancing. The results of this work suggest future steps for realizing a complete LFA, and discuss elements of the accelerometer which will affect its performance. In Chapter 2, the mechanics of particle trapping with a laser beam are discussed as an introduction to the LFA concept. Several optical effects which affect performance are also presented. Chapter 3 develops the concept of optical force rebalancing and its use in the LFA, and outlines its major advantages and limitations. Chapter 4 describes the experimental apparatus used to demonstrate the feasibility of the LFA and obtain preliminary performance diagnostics. Descriptions of laser sources and important electro-optic components are included. The results of demonstrations of particle trapping in high vacuum and optical force rebalancing are covered in chapter 5. Preliminary performance diagnostics for a constant 1 g acceleration, including short term sensitivity and bias stability, are also presented. Chapter 6 concludes the thesis by proposing future steps for realizing a complete LFA and testing its ultimate performance.

Chapter 2

Optical Trapping

2.1 Origins of Optical Trapping

With the invention of the laser in the early 1960s, high intensity and high gradient light sources became easily attainable in a laboratory. Later in the decade, physicist Dr. Arthur Ashkin of Bell Laboratories calculated that a laser beam focused onto a microscopic particle could exert a large force through radiation pressure, or the transfer of momentum from light to a reflecting surface [Ash97]. Soon after, Ashkin experimentally demonstrated that laser light would not only push small latex spheres in a fluid, but could also confine them within the beam. A combination of two counter-propagating laser beams created the first three-dimensional optical trap with a micron-sized latex microsphere suspended in water [Ash70]. In 1971, Ashkin levitated a 20 μm glass sphere in air (against gravity) with a single vertical laser beam (shown in figure 2-1), and reported stable trapping for many hours [Ash71].

The achievements of these experiments availed a new method for the clean and precise manipulation of microscopic particles. Extensions of these techniques have made a significant impact in other fields, including biology and atomic physics [Chu85], [RaP87]. The use of 'optical tweezers,' as this method is called in biology, have made studies of microscopic biological systems like RNA-DNA transcription and the fusing of cells possible [Fin94]. In physics, the trapping of neutral particles led to the discovery of atom trapping techniques, known as laser cooling, and major advancements in high precision atomic spectroscopy and atom interferometry [Kas89], [DaK95].

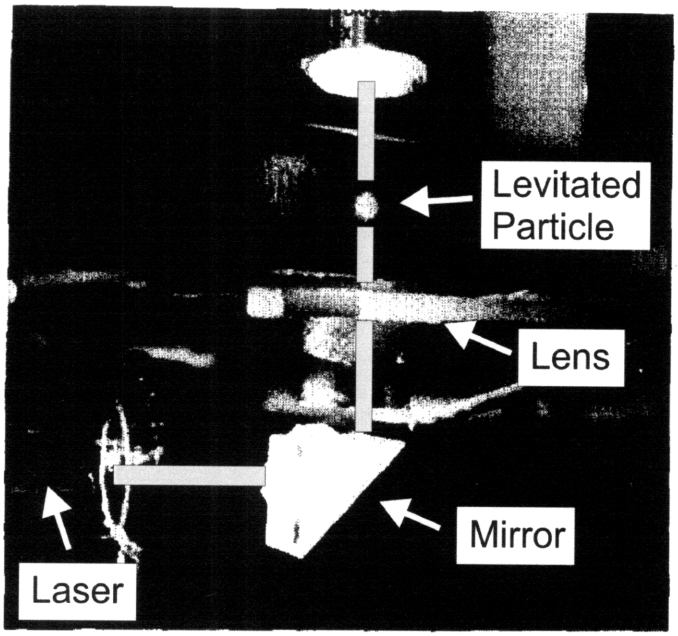

Figure 2-1: A 20 μm glass sphere levitated by a focused laser beam. Photograph taken at Bell Laboratories in 1971. Adapted from[Ash71] (beam path added for clarity).

2.1.1 Application to inertial sensing

One of the important later achievements in the optical levitation of glass particles was trapping in high vacuum, where viscous drag and other thermal effects are negligible [Ash76]. Ashkin reported that, "If the viscous damping [of air] can be further reduced, applications to inertial devices such as gyroscopes and accelerometers become possible" [Ash71]. No sensor development was pursued for such an application, however, because of the state of laser and vacuum technology at the time. Subsequent advancements in both fields, however, renewed interest in precise sensors using levitated dielectric particles. The light force accelerometer (LFA), which uses a levitated microsphere as a proof mass, is an example of such an instrument. Before presenting the LFA concept, however, a description of the optical trapping of neutral particles is in order.

2.2 Mechanics of optical trapping

The system of interest for optical trapping is a spherical dielectric particle placed in a Gaussian-like laser beam. A basic ray optics model of light reflection and transmission

through the sphere illustrates how the laser beam confines the sphere within the beam and accelerates it in the beam direction[1]. By breaking up a laser beam into individual rays and modeling their reflection, refraction, and transmission at the surface of a particle, one can determine the transfers of momentum from light to the particle.

Consider a dielectric sphere with index of refraction n in a gas with index m, and that $n > m$ (otherwise, particles will be forced out of the beam rather than trapped). Figure 2-2 diagrams the forces exerted to a sphere when a ray of power P meets the surface of a dielectric sphere at an angle θ_i from the normal. The first force is due to reflection (also known as radiation pressure)[2]. A component of the ray is reflected with power PR, where R is the Fresnel reflection coefficient (assuming the ray is unpolarized):

$$R = \frac{1}{2}(R_S + R_P) = \frac{1}{2}\left(\left(\frac{\sin(\theta_t - \theta_i)}{\sin(\theta_t + \theta_i)}\right)^2 + \left(\frac{\tan(\theta_t - \theta_i)}{\tan(\theta_t + \theta_i)}\right)^2\right) \tag{2.1}$$

R_S and R_P are the reflection coefficients for polarization components in and out of the plane of incidence and θ_t is the angle of the transmitted ray relative to the normal (defined by Snell's law). The incident ray has a momentum of $\frac{mP}{c}$ per second, and upon reflection a component of this momentum is imparted to the sphere. The magnitude of the force is dependent on the incident angle θ_i, and is a maximum of $2\frac{mP}{c}$ for a complete retro-reflection (when $\theta_i = 0$). Since the sphere is in the center of the beam, a symmetrically situated ray exerts a force of the same magnitude. The radial components, however, cancel out and the net force points along the direction of the beam ($+z$); thus, the reflective force accelerates a particle along the beam axis.

Another portion of the ray is transmitted with power PT, where T is the Fresnel transmission coefficient ($T = R - 1$). As the right side of figure 2-2 shows, the transmitted ray is refracted and deflected toward the center of the beam. To conserve momentum, a force is exerted on the sphere away from the beam axis ($-r$). A symmetric ray cancels out this

[1]It should be noted that the ray optics model presented here is accurate for particles which are much larger than the wavelength of the light. As will be seen, this assumption is appropriate for microspheres used in the light force accelerometer. For particles which are small compared to the wavelength, however, this description breaks down. Rayleigh particles, as they are known in the literature, act like basic dipoles and cannot be treated with a simple ray picture.

[2]In the literature, this force is commonly called the scattering force, since for more sophisticated analysis the light is scattered by dipole radiation. 'Reflective' force is chosen here since it is appropriate for the discussion here.

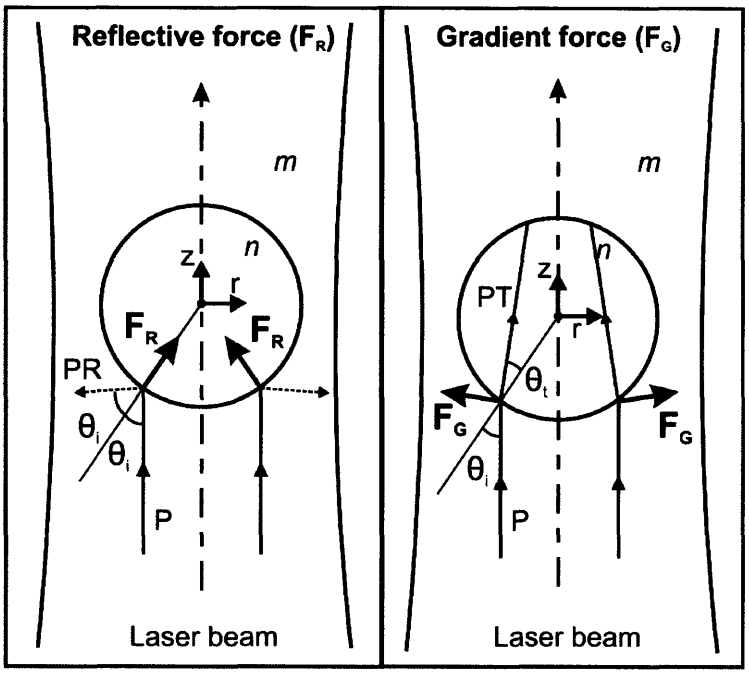

Figure 2-2: Diagram of the reflective and gradient forces on a dielectric sphere.

radial force, as shown in the diagram. This force will be referred to as the gradient force, since it is produced by the focusing of the beam through the sphere[3].

To demonstrate how these forces can trap a spherical particle in a laser beam, consider the case when the particle is radially displaced from the axis of the beam. Figure 2-3 shows the reflective and gradient forces from rays symmetrically situated about the particle. As was just shown, the net reflective force due to each ray ($F_{R1}^{i,o}$ and $F_{R2}^{i,o}$) is in the direction of the laser beam. The radial components for the input and output rays roughly cancel out (e.g., F_{R1}^{i} cancels out F_{R1}^{o} in the radial direction); the sum of the gradient forces, however, produces a net radial force. While the force vectors for the rays 1 and 2 are radially symmetric, beam 1 contains significantly more power (it is closer to the center of the beam). Therefore, $F_{G1} > F_{G2}$ and the net force points in the $-r$ direction (see the sum of forces diagram in figure 2-3). If the particle were displaced to the other side of the beam, the net gradient force would also point toward the center of the beam. It is now clear that a laser beam

[3]In the literature, this force is also referred to as the gradient force. The reason is clear when looking at the definition of this force on a Rayleigh particle, which is treated as a simple dipole: $F_G = -\frac{1}{2}\alpha m \nabla E^2$, where α is the polarizability of the particle, m is the particle mass, and E is the electromagnetic field of the light. The 'trapping' potential due to this force is simply $U_G = \frac{1}{2}\alpha m E^2$, so it is clear that a higher intensity beam ($I \sim E^2$) creates a deeper potential and stronger trap.

accelerates the particle along the beam axis and transversely traps it.

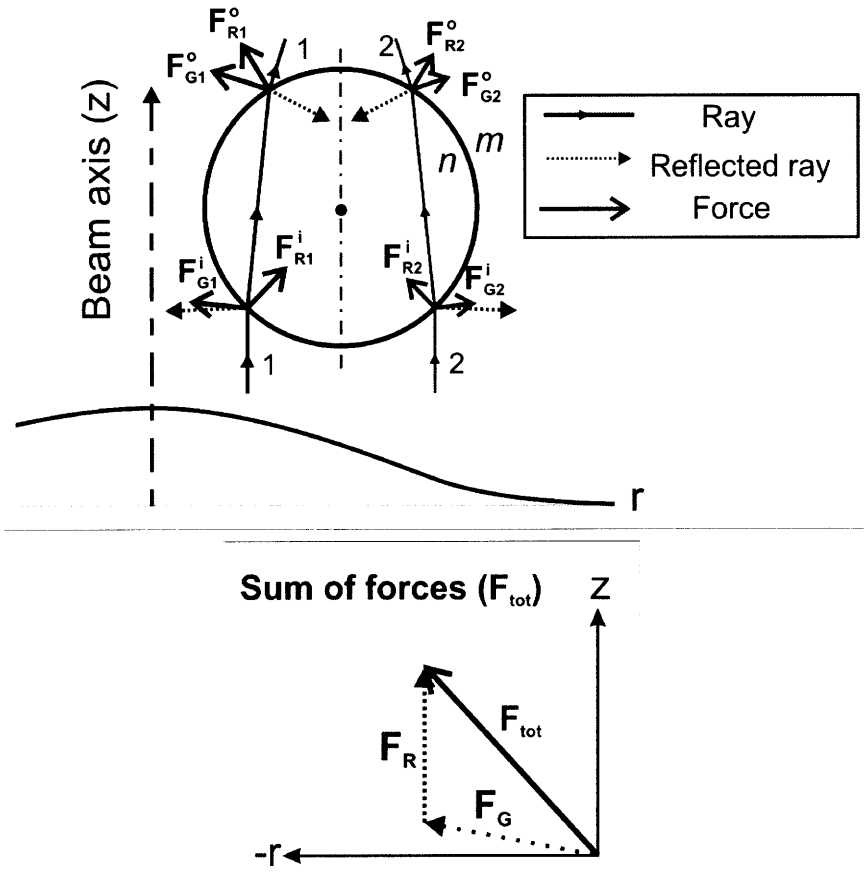

Figure 2-3: A ray optics diagram of a dielectric sphere in the presence of a laser beam. The curve below the sphere represents the power distribution in the laser beam.

To calculate the total force a ray exerts on a sphere, the reflective and gradient forces due to each reflection and transmission at the surface of the sphere must be summed. In general, a convenient representation of the net force components in the radial (r) and axial (z) is

$$F_r = Q_r \frac{mP}{c} \tag{2.2}$$

and

$$F_z = Q_z \frac{mP}{c} \tag{2.3}$$

where Q_r and Q_z are dimensionless factors dependent on θ_i and the relative index of the sphere and surrounding gas, n/m. F_r is roughly equal to the reflective force and F_z is roughly equal to the gradient force (it will be shown that it is more convenient to calculate the forces

along the axes). The total force on a particle exerted by a ray, therefore, is

$$F = Q\frac{mP}{c} = \sqrt{Q_r^2 + Q_z^2}\frac{mP}{c} \tag{2.4}$$

There are several methods for calculating Q, but the simplest is to sum up the force contributions for an infinite series of internal reflections and transmissions (see figure A-1). This derivation is somewhat tedious, and can be read in detail in appendix A.

It is interesting to consider the relative magnitudes of the reflective and gradient forces. Figure 2-4 shows each Q factor for a single ray hitting a particle at varying angle θ_i, calculated from equations A.4 in appendix A. Clearly, the total force exerted by a laser beam (made up of a distribution of rays) depends on the intensity distribution and convergence of the beam (e.g., if a lens focuses the beam on the particle).

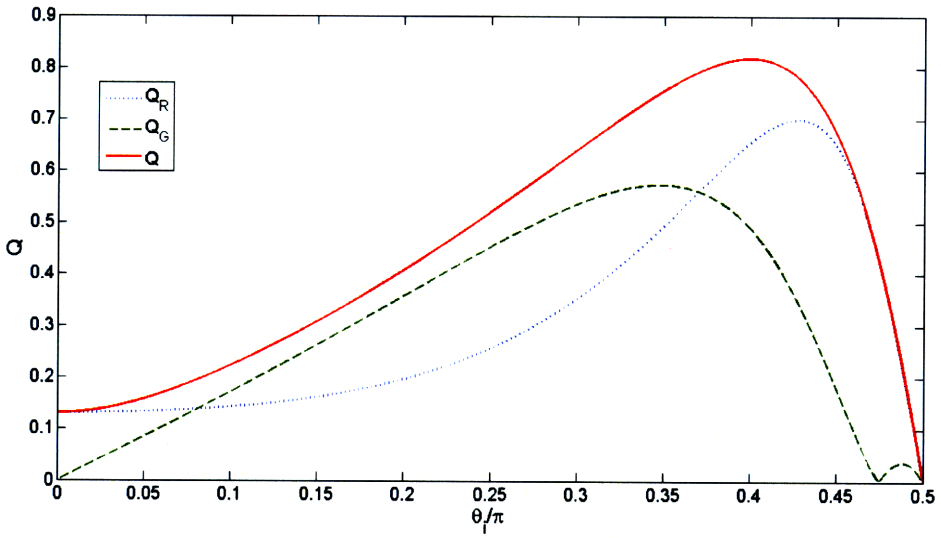

Figure 2-4: Light force scaling factors Q_r, Q_z, and Q as a function of θ_i, with a relative index of $n/m = 1.45$.

The discussion of optical forces in this section can account for the behavior of a dielectric sphere trapped in a laser beam when the surrounding gas is at atmospheric pressure or high vacuum. In between these pressure regimes, however, other thermal effects related to the absorption of light in the sphere, known as photophoretic effects, contribute significantly to the dynamics of the trapped sphere.

2.3 Photophoretic Effects

The absorption of light by a particle results in heating of the particle and the surrounding gas. When this heating occurs non-uniformly, the gas exerts a force on the particle[4]. For a spherical particle in a laser beam, it is possible for heating to be dominant on the incident or far side. The photophoretic force then points along the beam axis and either adds to radiation pressure ('positive' photophoresis) or opposes it ('negative' photophoresis) [Plu85]. Furthermore, the overall magnitude of the force is strongly pressure dependent. In the limit of high vacuum, of course, there is no photophoretic force. This section serves to provide an understanding of these effects, since these forces contribute to significant biases in the LFA.

The theory of aerosol mechanics has developed a basic description for the photophoretic force on a spherical particle in a laser beam. The force is represented as

$$\vec{F}_R = -\frac{4\pi R \eta_e^2 J K}{\rho_g T_S K_i} \vec{I} \tag{2.5}$$

where R is the particle radius, η_e is the gas viscosity, K is the coefficient of thermal slip (~ 1), T_S is the surface temperature, ρ_g is the density of the external gas, K_i is the internal thermal conductivity, and $\vec{I}$ is the intensity on the particle [Yal76]. The most important factor in the equation, however, is the dimensionless factor J. J measures the non-uniformity of the intensity distribution within the particle, and is proportional to the absorption efficiency of the particle material (capturing the spectral properties of the effect). Ultimately, this factor determines whether negative or positive photophoresis occurs.

The formula in equation 2.5 is only accurate in the regime where the mean free path of the surrounding gas is much smaller than the particle size (e.g., atmospheric pressure), but the model can be extended to low and high pressure by a scaling law

$$g(K_n) = \frac{1}{1 + 3C_m K_n} \frac{1}{1 + 2C_t K_n} \tag{2.6}$$

where K_n is the Knudsen number, or the ratio of mean free path to the particle size (proportional to $1/p$, where p is the pressure) and C_m and C_t are empirically determined coefficients

[4]Photophoretic effects apply in much larger systems as well. These forces are thought to be the source of particle depletion around stellar bodies [WuK05], and are potentially strong enough to 'levitate' particles in the Earth's atmosphere[Arn82].

(typically $C_m \sim 1$ and $C_t \sim 2$) [Ree77]. The pressure-dependence of photophoretic force is plotted for a range of K_n in figure 2-5. Clearly, this effect peaks when the mean free path is comparable to the particle size ($K_n \sim 1$). In this critical pressure regime, a particle may be destabilized and ejected from a laser beam. Thus, photophoretic forces may generate bias and stability problems in the light force accelerometer.

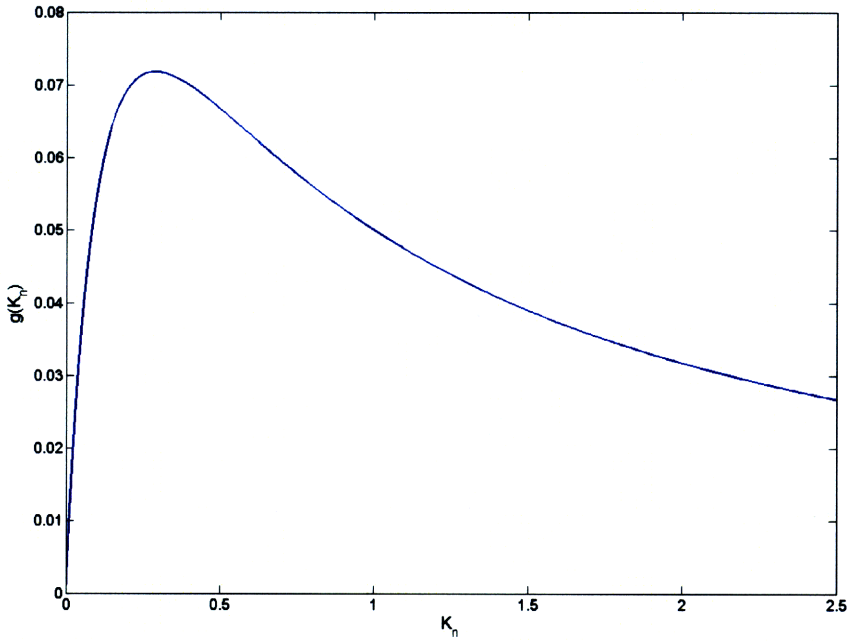

Figure 2-5: Plot of the scaling of photophoretic force as a function of the Knudsen number, K_n ($\sim 1/p$).

A spherical particle in a laser beam will focus light, leading to higher absorption on the far side of the particle (as shown on the left in figure 2-6). This indicates that gas heating on the far side will lead to negative photophoresis. Exact modeling of the intensity distribution inside a 10 μm sphere (shown on the right in figure 2-6) verifies that absorption and therefore heating are greatest on the far side of the particle[5]. As will be discussed in the results of this work, experiments with glass microspheres trapped in a laser beam observed significant negative photophoresis. While beam shaping or selection of larger or smaller particles may

[5]This plot was produced by a simulation of electric field distribution in a homogeneous sphere, using a rigorous derivation from classical Mie theory. Mie theory solves the problem of a plane wave scattered by a homogeneous sphere, and provides exact solutions of the internal and external fields. While the derivation and presentation of these results is beyond the scope of this chapter, they can be found in several sources [VDH81] (Chapter 9), [BAS88], [BAS89].

influence the magnitude of photophoretic effects, the simplest way to reduce them is to use a low absorption material like fused silica glass.

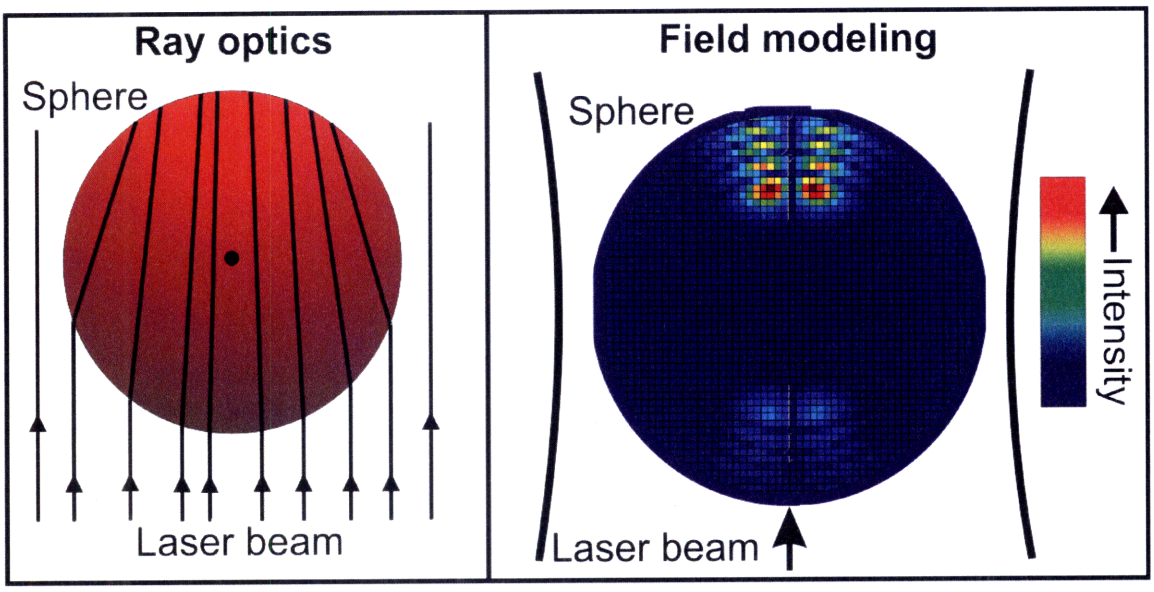

Figure 2-6: Basic ray optics (left) and exact field modeling (right) show higher intensity and absorption on the far side of a sphere, indicating that photophoretic forces opposing radiation pressure should occur.

2.3.1 Other significant optical effects

Finally, a few optical effects which could influence trapped particle behavior are included for reference in later chapters. The discussion of optical effects thus far has not addressed another result of absorption in a particle. When circularly polarized light is absorbed in a particle, a torque is exerted on it. The classical interpretation is that angular momentum in an electromagnetic wave is absorbed and transferred to the particle as mechanical angular momentum. The quantum mechanical picture describes photons as having 'spin' angular momentum in integer amounts of $\sigma_z \hbar$ ($\sigma_z = \pm 1$), which is then transferred to the absorbing medium as mechanical angular momentum. The torque on an absorptive particle is

$$\Gamma = \frac{P_{abs}}{\omega} \sigma_z \tag{2.7}$$

where ω is the frequency of the laser and P_{abs} is the absorbed power [Fri96]. The absorbed power is a function of the optical power and the absorption coefficient, which is about

10^{-5}cm^{-1} for 1 μm light in fused silica glass. If rotation of a particle is undesired, then linear polarization must be maintained. In principle, a trapped particle in vacuum may continue to accelerate to extremely high frequency, since there would be no viscous drag [Ash74]. For irregularly shaped particles, rotations may lead to instability and ejection from the laser beam.

The last optical effect considered here involves internal optical resonances known as 'whispering gallery modes' (WGMs), which could alter the force of light on a spherical particle when excited. In a glass sphere, light may couple into internal modes when the circumference of the sphere is equal to an integer numbers of wavelengths. In a micron-sized sphere, these resonances are very sharp and may achieve quality factors as high as 10^9. WGMs, therefore, may provide a tool for precise measurements of particle size if a mode can be locked to with the laser frequency. However, if the frequency of a freely running laser drifts across a WGM resonance, the power coupled into the sphere is suddenly increased. As a result, the optical trapping forces exerted by the laser beam would change. In the light force accelerometer, this would generate large biases. The next chapter will address this and other potential limitations in the accelerometer concept.

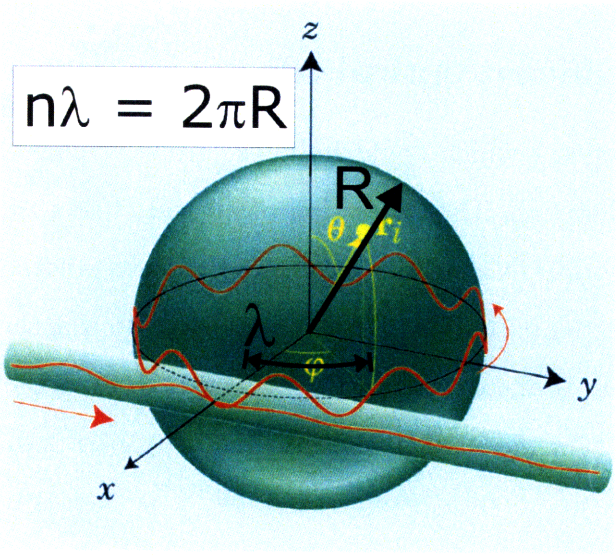

Figure 2-7: Whispering gallery modes (WGMs) are excited by coupling light via internal reflection into the circumference of a spherical particle. Adapted from [AHV03].

Chapter 3

Light Force Accelerometer Concept

This chapter presents the principles of the light force accelerometer (LFA) concept and discusses some of its notable advantages and limitations. The discussion focuses on the essential functions of the accelerometer, and how a high sensitivity sensor could be built from them.

The LFA concept was motivated by demonstrations of the optical levitation of glass microspheres, and the proposal by Arthur Ashkin that precise inertial sensors could be made from a system using a levitated dielectric particle as a proof mass [Ash71], [Ash77]. While the pursuit of such a sensor was limited by the state of laser and vacuum technology, rapid advancements in compact, high power laser sources and electro-optic technology during the last 30 years has made it feasible to develop a compact LFA [Kel05].

3.1 Optical force rebalancing

The LFA measures acceleration through optical force rebalancing, or the rebalancing of inertial forces on a levitated proof mass by radiation pressure from a laser beam. As discussed in chapter 2, a laser beam both accelerates a dielectric sphere along its axis (radiation pressure, or reflective force) and transversely confines it within the beam (gradient force). A stable trap can be created, as was done in Ashkin's work, by placing a glass microsphere in a vertical laser beam with sufficient power for radiation pressure to balance gravity. Without the presence of gravitational forces, a trap can be formed by placing a sphere within two counter-propagating beams, as shown in figure 3-1. This configuration allows for a single-axis

accelerometer to operate in any orientation.

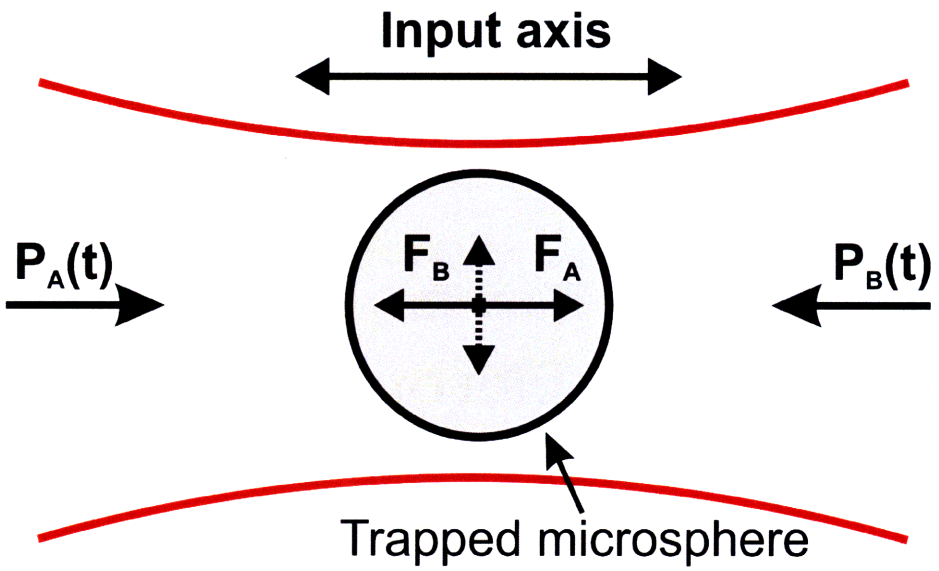

Figure 3-1: Diagram of a stable two-beam trap with which optical force rebalancing is realized. The dashed lines represent gradient forces from both beams.

To enable rebalancing, the proof mass position must be measured along the beam axis (also the input axis). Interestingly, this can be accomplished with the light reflected off the proof mass. Figure 3-2 shows how light is reflected perpendicularly to the laser beam from a levitated sphere[1]. This reflected image is then focused onto a split photodetector, as shown in a diagram of the rebalancing loop (figure 3-3). The detector provides the reference position, or set point, for rebalancing. The normalized difference signal from the detector (difference between the upper and lower signal divided by their sum, Δ/Σ in figure 3-3) is proportional to particle displacement, and is used to maintain the particle position by adjusting the beam powers with variable optical attenuators (VOA).

If there is no net force on the sensor, equal powers in beams A and B will maintain the particle position (left, figure 3-4). When a force F is applied to the sensor, the proof mass position is maintained by proportionally increasing the power in beam A (right, figure 3-4). Equilibrium is reached when the difference in the reflective force of the beams balances F (i.e., $F_A - F_B = F$). Since the magnitude of the reflective forces is proportional to the power of a laser beam, acceleration may be calculated from the power difference of the

[1]The reflection from the bottom surface of the particle and the transmission from the top surface actually create two spots (a and b in figure 3-2). For small particles, however, these two spots are difficult to resolve because they are spaced approximately one particle diameter apart.

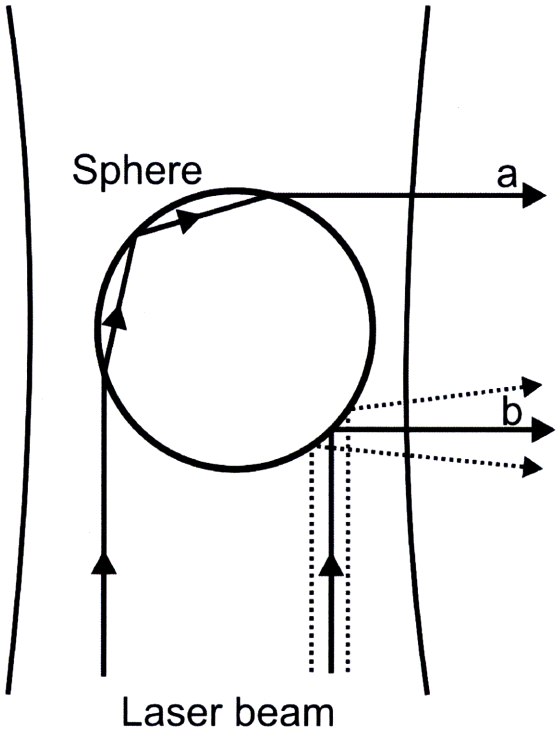

Figure 3-2: A ray optics diagram of reflected light that forms a spot for particle position measurement on a split photodetector.

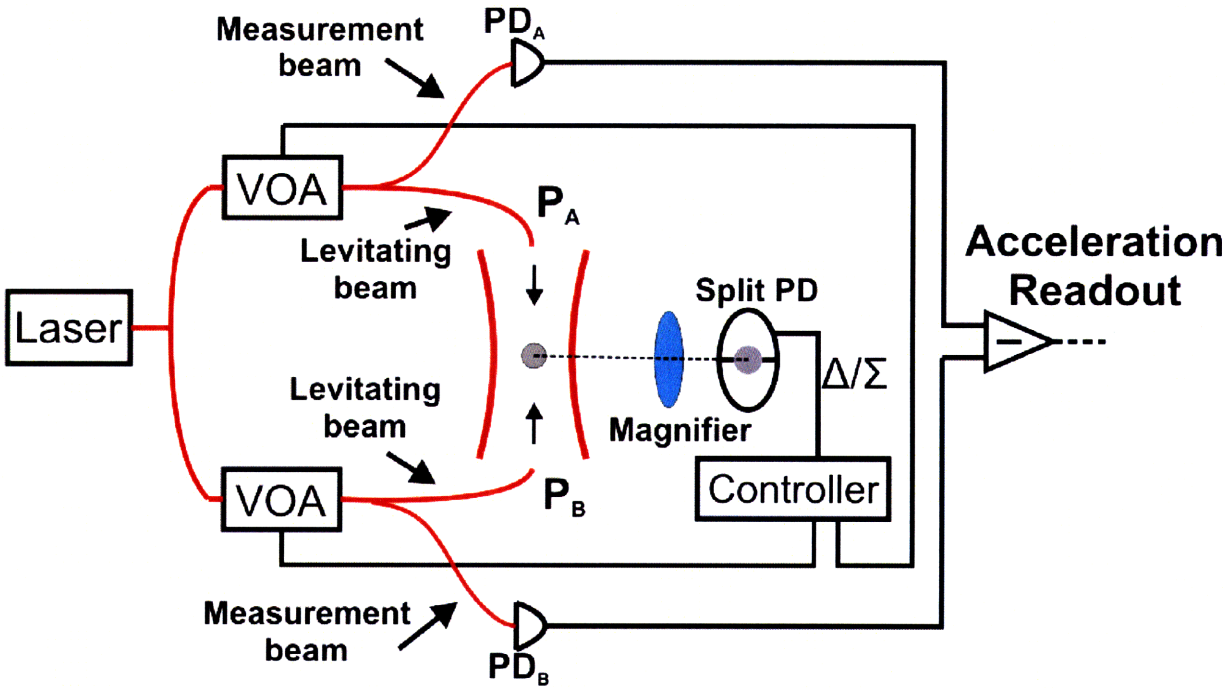

Figure 3-3: Diagram of the LFA optical rebalancing loop. The acceleration readout of the sensor is the measured difference between the power signals P_A and P_B on detectors PD_A and PD_B.

beams($P_A(t) - P_B(t)$). The accelerometer readout, or the output signal of the sensor, is measured as the difference between the photodetector signals PD_A and PD_B, as indicated in figure 3-3.[2].

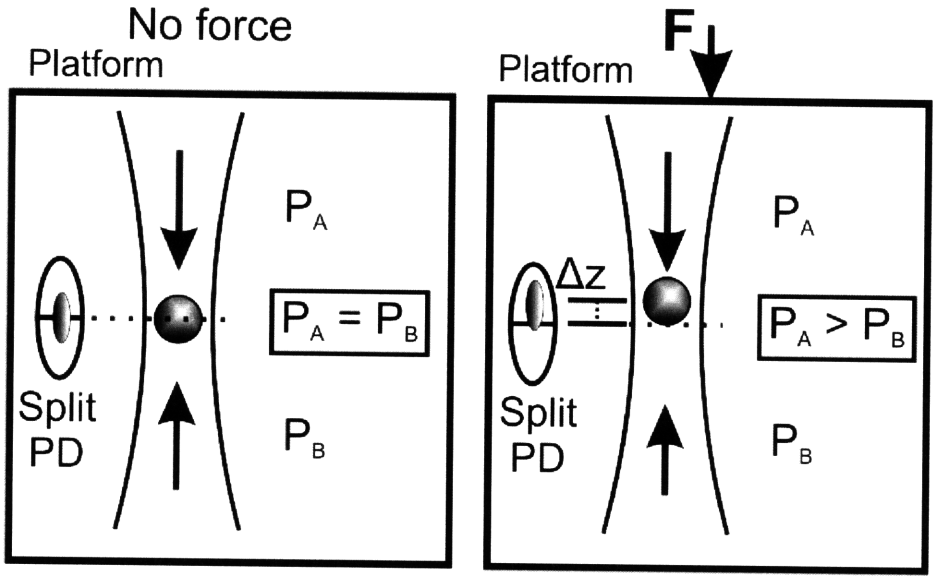

Figure 3-4: Optical rebalancing for zero input (left) and a force F along the beam axis (right).

3.2 Advantages of the LFA

The expected performance of the LFA will now be addressed. Several salient features of the LFA concept make it capable of high sensitivity and scale factor stability. These advantages arise from the noise statistics of the acceleration measurement and the potential for continuous recalibration in a device. A brief description of these factors is included below.

3.2.1 Accelerometer noise statistics

Optical force rebalancing provides a low noise acceleration measurement when a levitated sphere is trapped in high vacuum. Considering a simple case where a glass sphere is levitated by a single laser beam against a constant 1 g acceleration, the fractional noise in a measure-

[2]Note that portions of the light going to the proof mass in beams A and B are measured (the measurement beams), rather than the actual powers incident on the particle. Still, the measured power difference is proportional to F.

ment of g is equal to the fractional noise in measurement of the steady-state levitating beam power P_0:

$$\frac{\delta g(t)}{g} = \frac{\delta P(t)}{P_0} \tag{3.1}$$

where $\delta g(t)$ is the RMS value of the acceleration measurement and $\delta P(t)$ is the RMS value of the measured optical power. While a detailed noise statistics analysis is beyond the scope of this chapter, a simple model of noise processes including laser relative intensity noise and shot noise for the measurement of the levitating beam power shows that the laser noise integrates down as 1/(measurement interval) to the shot noise limit [Sto05]. Figure 3-5 plots the expected acceleration error for this single-beam LFA when the proof mass is levitated in high vacuum (where Brownian noise and photophoretic forces are eliminated). Neglecting other noise processes, the LFA was estimated to attain under 10 ng of measurement error in only 10 seconds of averaging, which is a precision comparable to a demonstrated cold atom gravimeter [PeC01]. While a real system will probably not achieve this ideal performance, the LFA is a considerably simpler system and is much easier to shrink to a compact sensor than a cold atom instrument.

3.2.2 Scale factor linearity

Like other force feedback or rebalancing accelerometers, the LFA should achieve a linear scale factor over a large range of acceleration (dynamic range). The dynamic range of the LFA depends primarily on the total power available for rebalancing, which is proportional to the maximum reflective force that one of the laser beams could exert on the levitated proof mass. The scale factor of the LFA is the ratio of the optical power required for rebalancing per unit acceleration. Nonlinearities in scale factor arise when the proof mass heats and expands from absorption. Scale factor will decrease as a particle expands, since it will reflect more light and thereby require less optical power to rebalance. This nonlinearity may be avoided in practice by maintaining the total power in both beams so that the total absorption does not change (rebalancing would simply redistribute the power between the beams).

Another source of scale factor nonlinearity is the coupling of light into whispering gallery modes (see section 2.3.1 for a basic discussion of these resonances). This effect is negligible for small spheres (5-20 μm range), but is potentially significant for particles greater than

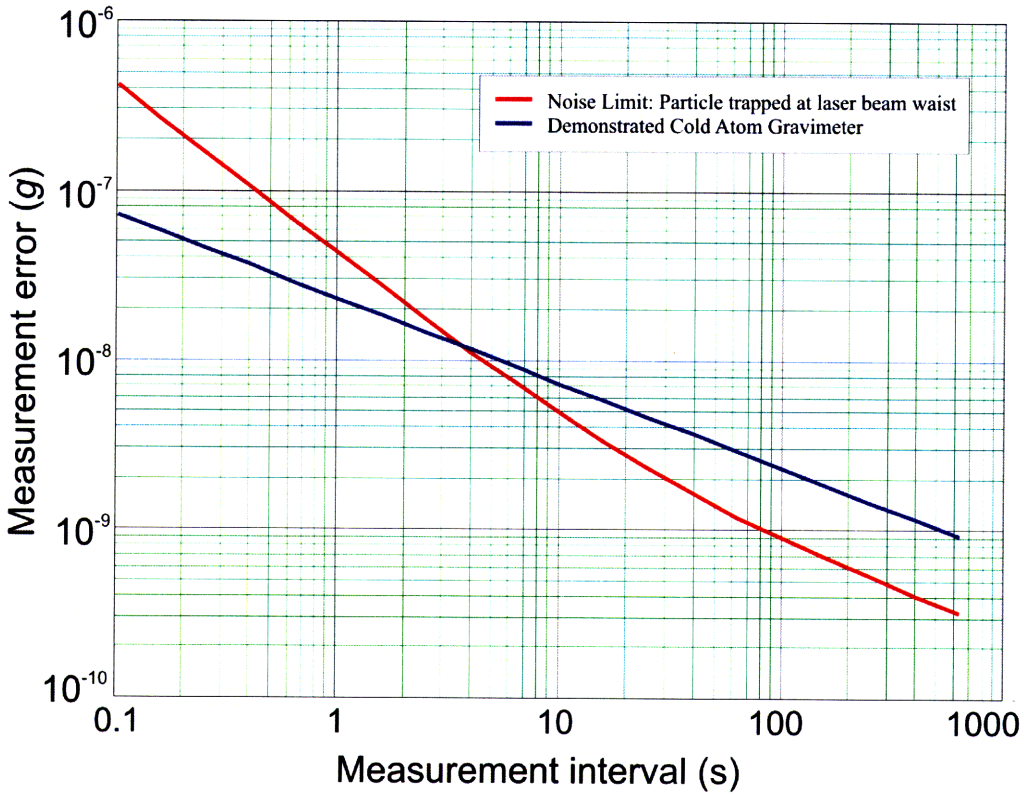

Figure 3-5: Theoretical precision of a LFA with a particle trapped at the beam waist. For comparison, experimental results from a demonstrated cold atom gravimeter are plotted. Adapted from [Sto05].

500 μm. Whispering gallery modes in glass microspheres achieve some of the highest quality resonances known ($Q \approx 10^9$, [Ver98]). Excitation of a WGM would decrease the amount of reflected light, requiring more incident power for rebalancing the same inertial acceleration. Fortunately, these effects may be avoided by active laser frequency stabilization or ensuring the laser frequency remains between these broadly separated resonances. For instance, a 10 μm sphere has circumferential whispering gallery modes spaced by $\delta\nu = c/(2\pi D) \approx 4.7$ THz. Since most laser frequencies are stable to a band much smaller than this spacing, a particle would need to nearly double in size before the next resonant mode would be excited (for a thermal coefficient of < 1 ppm/°C in silica glass, this is not possible).

3.2.3 Scale factor stability and continuous recalibration

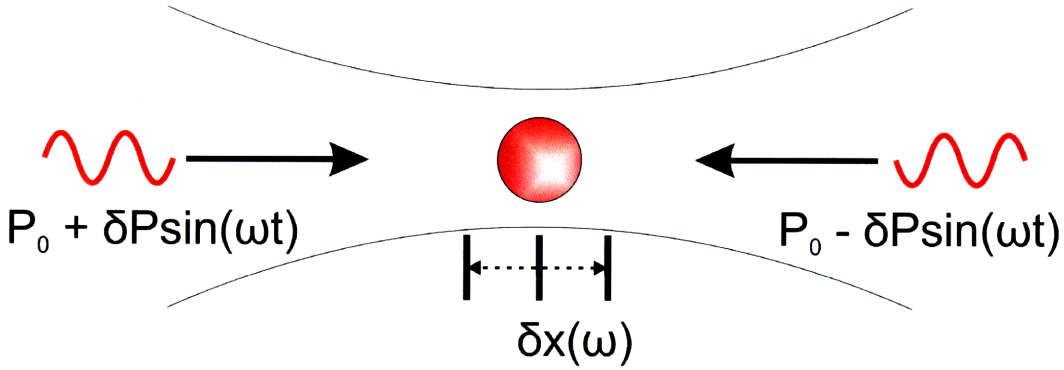

Figure 3-6: Diagram of continuous scale factor recalibration concept.

While optical rebalancing should provide a linear scale factor over a large dynamic range, it does not necessarily guarantee long term stability. Scale factor drifts may occur because of long term drifts in electronics (e.g., amplifier gain drifts). These drifts can be measured and used to calibrate acceleration measurements continuously with the following technique.

Calibration is achieved by dithering both levitating beam powers at frequency ω, as shown in figure 3-6). The proof mass will oscillate in response. With continuous measurements of its average oscillation amplitude, $\delta x(\omega)$, and the fractional power amplitude, δP, the scale factor may be updated (the frequency of the dither, ω, would be made faster than vehicle dynamics and the accelerometer bandwidth). Quantitatively, the scale factor is related to

these amplitudes by

$$K = \frac{\delta P}{\delta \ddot{x}(\omega)} \tag{3.2}$$

The proof mass response is represented by a simple second order system

$$m\delta\ddot{x}(\omega, t) = m(\delta x)\omega^2 cos(\omega t + \phi) = \frac{n\delta P}{c} cos(\omega t) \tag{3.3}$$

where m is the particle mass, $\delta\ddot{x}(t)$ is the particle acceleration due to the dither, n is the surrounding gas index of refraction, and c is the speed of light. Therefore, the precision of a scale factor measurement ultimately depends on the resolution of particle position and the optical power amplitude (δP). Both of these signals are measured on photodetectors, so the fundamental noise limit is shot noise in each case. The fractional uncertainty in scale factor measurement is

$$\frac{\Delta K}{K} = \sqrt{\left(\frac{\Delta(\delta x(\omega)}{\delta x(\omega)}\right)^2 + \left(\frac{\Delta(\delta P)}{\delta P}\right)^2} \tag{3.4}$$

where ΔK, $\Delta(\delta x(\omega))$, and $\Delta(\delta P))$ are the RMS noise values of the scale factor, position and power dither amplitudes, respectively. Assuming that the each measurement is shot noise-limited, and that the power of the particle image focused on the split photodetector is 15 μW, scale factor resolution is limited to $0.1\text{ppm}/\sqrt{\text{Hz}}$. For continuous recalibration, the resolution is equivalent to scale factor stability.

3.2.4 Radiation hardness

While system survivability in the space environment is not an immediate concern in this work, it is worth noting that the optical components of a LFA are intrinsically radiation hard. Most optical components in the system have been extensively tested for previous spaceflight programs, and it is likely that the LFA would serve well as an inertial sensor for spacecraft navigation.

3.3 Concept Limitations

A few potential limitations of the LFA deserve mention before a description of the current apparatus in the next chapter. Several few practical issues present interesting challenges for

the design of a deployable LFA. The following factors will play a significant role in the design of both the current experimental apparatus and future devices.

3.3.1 Reproducible particle launching

The process of placing a particle in a laser beam has been absent from discussion so far, but it will become a complex issue in developing an accelerometer. Glass microspheres are difficult to manipulate once deposited on a surface, due to a strong Van der Waals attraction. Spheres smaller than 10 μm in size easily aggregate, or stick together. This effect can be mitigated somewhat in a fluid, and it is for this reason that the first optically trapped microspheres were captured in fluids. To make precise measurements, however, it is best to levitate particles in high vacuum. Dry particle samples, unfortunately, require a significant force to extract them from a flat surface (e.g., a glass slide). Furthermore, it is difficult to both free and launch microspheres directly into a laser beam. In an actual sensor design, this will have an effect on starting time and potential 'blackouts' if a particle is lost from the laser beam. Using larger particles will reduce the magnitude of the Van der Waals attraction, and less force will be required to launch them from a surface. For applications where higher inertial inputs are expected, however, there is a large power cost for levitating larger particles (the levitating power grows as R^3, where R is the particle radius). Reproducible particle launching is expected to be the primary limitation in achieving a deployable sensor.

3.3.2 Transverse oscillations

In a two-beam configuration, particle position control is practically limited to motion along axis of the beam. Transverse impulses to a trapped microsphere, however, could lead to persistent oscillations while trapped in high vacuum. Scale factor stability would degrade during these oscillations, since as a particle moves radially from the center of the beam, there is less radiation pressure. Rebalancing would then require more incident power for the same acceleration. One potential solution is to damp oscillations with an orthogonal pair of laser beams. This would introduce cross-coupling effects (the gradient force of one beam pair is aligned with the reflective force of the other), but might avoid long term scale factor instability from underdamped oscillations.

3.3.3 Polarization dependence and other optical disturbances

Optical disturbances due to photophoresis and coupling to whispering gallery modes can be mitigated, as previously discussed, by trapping microspheres in high vacuum and tuning the laser frequency away from whispering gallery mode resonances. The polarization of the laser beams should also be controlled for trapping in vacuum. As discussed in section 2.3.1, circularly polarized light exerts a torque on levitated particles when they absorb light. At atmospheric pressure, rotations are damped by viscous friction; in high vacuum, however, linear polarization must be preserved to prevent undamped rotations from accelerating. While particle rotation may gyroscopically stabilize a particle, it could also create substantial variability in the reflected spot on the split photodetector if there are surface irregularities or contaminants[3].

3.4 Summary

The discussion of the accelerometer concept and some of the anticipated implementation issues will be applied to the experimental work discussed in the remainder of the thesis, which involved a demonstration of the essential functions of a light force accelerometer. The next chapter describes the apparatus used for these experiments, and is followed in chapters 5 and 6 by a discussion of current results and preliminary performance diagnostics, as well as suggestions for future work.

[3]If rotations are at a frequency above the bandwidth of the split photodetector, however, this effect is eliminated.

Chapter 4

Experimental Apparatus

4.1 Goals for experimental work

The goal of this thesis was to experimentally demonstrate the essential functions of a light force accelerometer in a laboratory bench-top system. This system serves to identify significant implementation issues, guide future development, and identify suitable applications for a LFA. As will be discussed in chapter 5, the current experimental apparatus demonstrated particle levitation in high vacuum and optical force rebalancing. This chapter describes the apparatus used for preliminary performance diagnostic experiments as well as important sensor design considerations related to present experiments. Recommendations for future modifications to the apparatus for improving performance and realization of a complete LFA are suggested in chapter 6.

4.2 Design of experimental apparatus

As described in the previous chapter, the LFA requires two counter-propagating beams for operation in any orientation. Since the objective of this thesis was to demonstrate particle trapping in high vacuum and optical force rebalancing, a two-beam system was not required. The simplest system that can achieve these objectives is a single vertical laser beam with sufficient power to levitate a glass microsphere in a 1 g field. A single beam system would also permit investigations of optical effects described in chapter 2 and allow preliminary tests of sensitivity and bias stability to be made. The only limitation of this configuration is that

it cannot measure performance parameters like fixed biases or scale factor for a range of inputs.

Figure 4-1 shows a basic diagram of the apparatus. The output of a laser is directed through a polarization controller and fast variable optical attenuator (FVOA) before being split into a levitating beam and a measurement beam (only several percent of the total power). The levitating beam is expanded and focused into a vacuum chamber, where glass microspheres are launched. As discussed in section 3.1, light reflected from a levitated microsphere can be focused onto a split photodetector for position measurement along the beam axis. The detector produces an error signal for the rebalancing loop, in which a digital controller adjusts the levitating beam power with an FVOA.

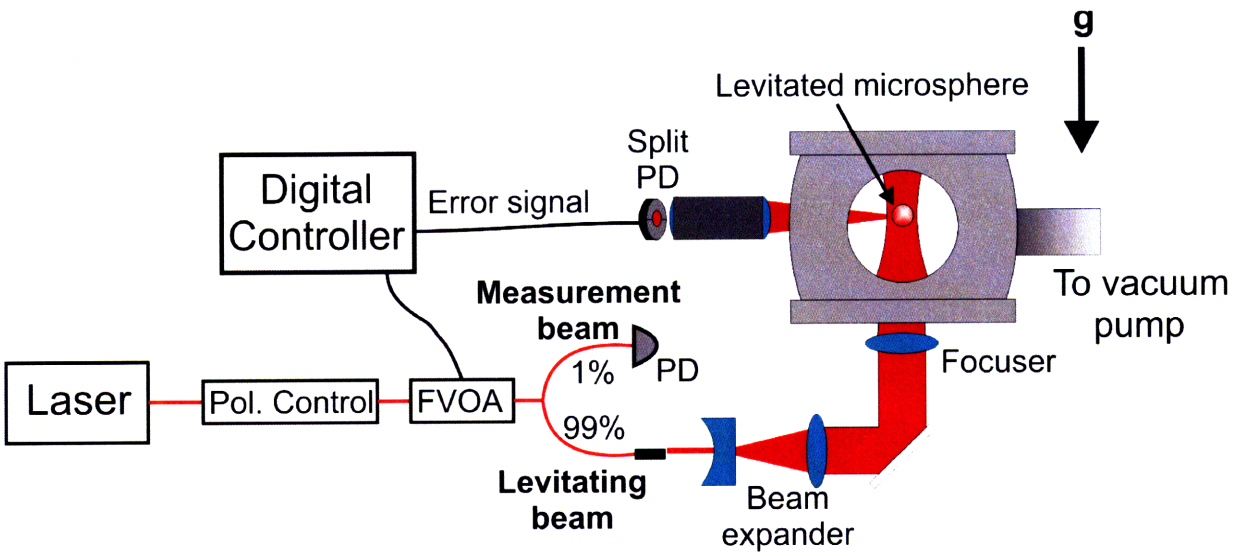

Figure 4-1: Diagram of the experimental apparatus used to demonstrate the feasibility of a LFA.

4.3 Laser sources

Several different laser systems were used in these experiments. As mentioned, the basic requirement for a laser source in the LFA is that it must provide sufficient power to levitate a particle against gravity. Simple calculations predict 60-100 mW of CW power are necessary to levitate 10-15 μm microspheres (assuming the beam is focused to a waist comparable to the size of a sphere).

While free-space optics could be used in experiments, fiber-coupled lasers offer superior alignment simplicity and stability and would be preferred in a compact device. In the last decade, fiber-coupled laser systems have become widely commercially available in compact, high power devices; extensive development of in-line fiber-optic and electro-optic components such as optical isolators, acoustic-optic and phase modulators, and optical attenuators has substantially eased control of laser power and frequency. Pump lasers, or lasers which are used to supply power to a high power amplifier, provide several hundred milliwatts of power for wavelengths around 1 μm. The primary laser used in this work is a grating-stabilized 980 nm diode laser. Two other laser systems were briefly implemented in experiments, but were found impractical for this preliminary demonstration. Their merits for further development are briefly discussed in section 4.3.2.

4.3.1 980 nm diode laser

A Bookham 980 nm diode laser provided more than adequate power (max of $\approx$300 mW at 400 mA of drive current) for levitating 10 μm glass microspheres[1]. Low-noise current and temperature controllers were used to operate the laser[2]. The simplest method for adjusting the levitating beam power is to directly modulate the drive current of the laser. Unfortunately, this introduces significant noise in the laser output. The laser also responds slowly to fast, large changes in drive current. To achieve the highest performance laser power control, which is crucial for optical force rebalancing, external attenuation of laser power with a fast variable optical attenuator was implemented (see below in 4.7.3). This allows the laser to operate with a steady drive current.

4.3.2 Other laser sources

With a maximum power output of 300 mW, the 980 nm pump can rebalance particle accelerations up to 2 g against the beam[3]. Levitation of larger particles was considered, which would have required substantially more power. Two other laser systems were included as candidates for particle levitation experiments.

[1]Bookham Inc., San Diego, CA, Model LC94 (InGaAs)
[2]ILX Lightwave LDX-3620 and LDT-5525 Models
[3]Of course, a single beam cannot force the particle to accelerate downward any faster than gravity.

Many powerful laser systems are available at the standard telecommunications wavelength 1550 nm. Low-noise distributed feedback (DFB) lasers are commonly used to pump erbium-doped fiber amplifiers (EDFA), which can produce several watts of continuous-wave power. In this apparatus, unfortunately, 1550 nm light is less convenient for levitating microspheres because it is invisible to standard silicon-based cameras, which only have reasonable quantum efficiencies for wavelengths up to 1100 nm. Visual monitoring of the vacuum chamber in the apparatus was crucial for launching particles. While InGaAs cameras will capture 1550 nm light, these cameras are typically much more expensive[4]. Experiments were made with an IPG Photonics EDFA (1.5 W) and ThorLabs TCDL M9 DFB laser (30 mW), but were prohibitively difficult because of poor visibility of levitated particles.

Another high power laser, an ytterbium-doped fiber laser, produces a single mode beam of 30 W at 1070 nm, another standard telecom wavelength[5]. Many standard optical components that are made for 1550 nm are also available for 1064 nm and 1330 nm. While the fiber laser was not used in the current work, it could be used to levitate larger microspheres in future experiments[6]. These high power laser sources, however, are less practical for applications in which electrical power is in shorter supply (e.g., spacecraft inertial navigation systems).

4.3.3 Beam-shaping optics

As shown in figure 4-1, the levitation beam is focused to provide sufficient incident intensity to levitate a microsphere. Free space beam-shaping optics comprise a compact Galilean beam expander and a single lens to focus the light to a waist over a distance of ~50 mm. Single mode 1064 nm fiber transmits a Gaussian-like beam, which can be focused to a waist determined by the relationship

$$w_o = \frac{2\lambda}{\pi}\left(\frac{f}{D}\right) \approx \frac{\lambda}{\pi}\left(\frac{1}{NA}\right) \tag{4.1}$$

where λ is the wavelength, f is the focal length of the primary lens, D is the diameter of the laser beam, and NA is the numerical aperture. The beam is expanded by a factor of $\approx 4-6$

[4]The best commercially available InGaAs cameras are made by Sensors Unlimited, Inc., which start at over $20,000.

[5]IPG Photonics, Inc. Model YLM-30

[6]There are a number of advantages to using larger particles. Their extra mass makes them less sensitive to laser random intensity noise and would allow for a significantly larger scale factor in an accelerometer

before focusing to a spot size of 10-12 μm. A beam profiler measured the beam waist and eased the design of the beam-shaping optics[7].

4.4 Microsphere selection and fabrication

The selection of microspheres for use as proof masses pose a few interesting challenges. Microspheres are made in a variety of glasses and polymers like polystyrene, and range in size from fractions of a nanometer to millimeter diameters. Frequently, these particles are produced in monodisperse (similar diameter) samples for optical tweezer experiments in fluids or as precise size standards in microscopy[8].

Microspheres composed of borosilicate glass and synthetic fused silica were chosen for low absorptivity[9]. As described in section 2.3, photophoretic forces can destabilize a levitated particle if significant absorption occurs. Ashkin et al. reported the occurrence of such behavior with levitated borosilicate particles in [Ash76]. Silica particles, which have an absorption coefficient of $\alpha \approx 10^{-5}\text{cm}^{-1}$ at 1 μm ($\sim$400 times smaller than the absorption in borosilicate glass), will reduce photophoretic effects when levitated[10]. This topic will be further discussed in the next chapter.

4.4.1 Fused silica particles and fabrication

Fused silica, also known as fused quartz, is a high purity synthetic glass that is commonly used in low-loss fiber optic systems. For experiments in this work, silica particles were first fabricated in the lab (the results of experiments with these spheres is discussed in section 5.1.2). An oxyhydrogen torch fused pulverized silica dust, which was fed via a pressurized line to the center of the torch flame. Heated beyond the softening point (around 1600°C), small silica particles fused and formed spheres through surface tension. Electroformed sieves selected samples of particles with diameters of 10-20 μm. Despite a low yield, each sample reliably produced particles which could be levitated with the 980 nm laser.

[7]Coherent Technology BeamMaster BM-3 profiler

[8]NIST approves certain samples as size standards for the microscopy community.

[9]Borosilicate particles made by SPI, Inc. (now Bangs Laboratories), Illonois. Silica particles made by Corpuscular, Inc., Cold Spring, New York.

[10]The absorption coefficient of a material is the factor of light attenuated per unit length of propagation in the material.

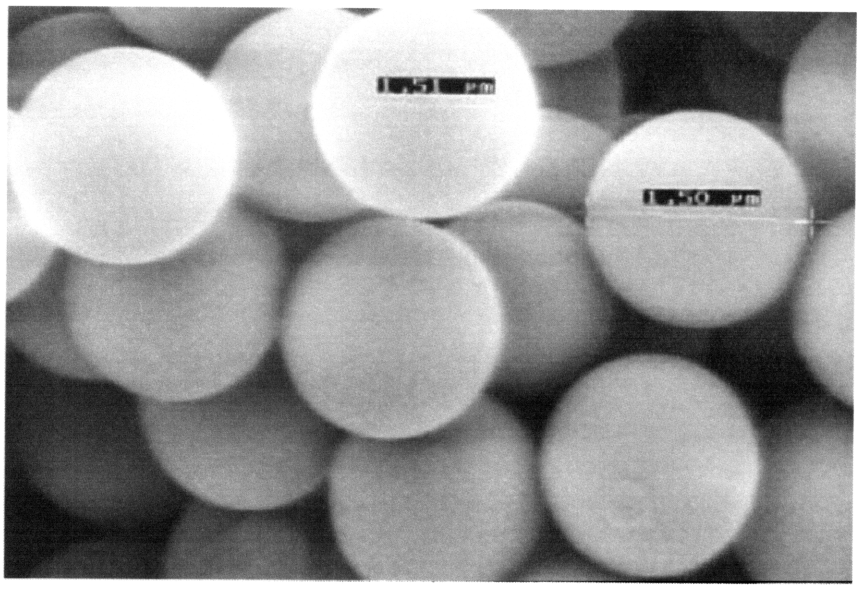

Figure 4-2: Scanning electron microscope image of 1.5 μm fused silica microspheres. [Corpuscular, Inc.]

This torch fusing method is commonly used for microsphere production, but monodispersity and sphericity are difficult to achieve. Furthermore, monodispersity is less important than sphericity for particle levitation experiments; aspherical particles may induce undesirable rotations and chaotic behavior (see section 5.1.1). More sophisticated methods used in the microsphere size standard industry produce more consistently spherical particles, as shown in figure 4-2.[11] The table below lists microsphere specifications for all samples used in experiments.

Particle Sample	**Diameter (μm)**	**Standard Deviation, μm (%)**
SPI Borosilicate	10	0.66 (6.6)
SPI Borosilicate	15	0.9 (5.8)
Corpuscular Fused Silica	10.6	1 (< 10)
Corpuscular Fused Silica	7.2	0.4 (< 6)

Table 4.1: Characteristics of microspheres used in experiments.

[11]For Corpuscular, Inc., Plain Silica NIST Size Standards

4.5 Particle Launching

To launch microspheres into a laser beam, many spheres are deposited on a glass slide (see figure 4-3). Since strong van der Waals forces stick spheres to the surface, the glass slide must be shaken to free them. This attraction may be as large as 10^4 times the gravitational force on a 10-20 μm particles. By fixing the slide to a structure with two piezo actuators and tuning them to excite cantilever resonances on the slide (at frequencies $\approx$29 kHz), microspheres are freed from the surface. As they migrate toward nodes of the oscillations, the focus of the laser beam is placed just above the slide. The slide is turned off once a particle is trapped. The entire process is manually executed by viewing the slide with a CCD camera.

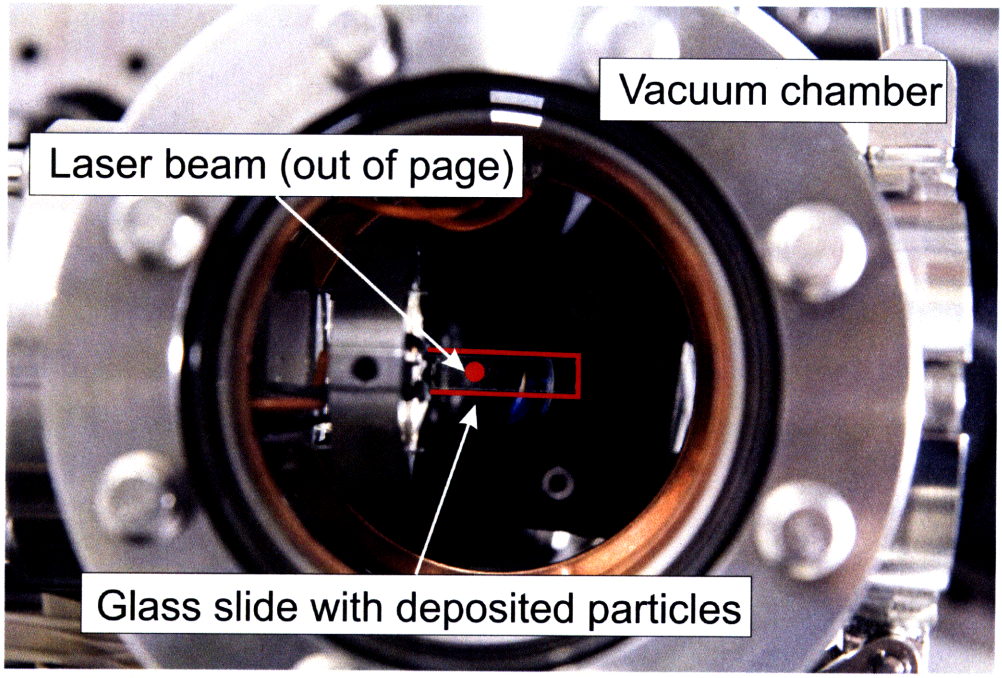

Figure 4-3: Picture of vacuum chamber from above. The slide is visible (outlined) with a distribution of particles on it. The laser beam is directed through the slide and out of the page.

The particle launching process is clearly random, and can require a few seconds to one minute to launch and levitate a microsphere. Viscous drag from air in the chamber aids in the launching process, since the large forces necessary to strip particles from the glass surface frequently give considerable momentum to particles upon their departure from the slide. For this reason, launching in vacuum is difficult and has not been achieved.

Future work for sensor applications will grapple with automating this process so that

particles can be reproducibly launched in a short time. Experimental design considerations regarding this subject are presented in chapter 6.

4.6 Vacuum system design

To levitate particles in high vacuum, the launching mechanism described above must be isolated in a vacuum chamber with optical access for the levitating beam and for a split photodiode to capture reflected light from a levitated particle for position measurement. To reduce the Brownian motion of a particle trapped in atmospheric pressure, the vacuum chamber must be pumped down to $< 10^{-1}$ torr. Photophoretic forces decrease roughly as the pressure and are negligible below $\approx 10^{-9}$ torr. A small chamber, shown in figure 4-4, was designed with four optical viewports, one electrical feed-through to supply the particle launching piezos, and one valved vacuum port[12]. Figure 4-5 diagrams the entire vacuum system. All ports were sealed with ConFlat® flanges, which are rated to hold vacuum at 10^{-13} torr with a clean system. The system was pumped down by a Pfeiffer roughing pump and thermomolecular turbopump. To reduce vibrations from the roughing pump, the vacuum chamber was fixed to a floated optical table and connected to the vacuum pump via a flexible stainless steel hose.

Since launching particles is easiest at atmospheric pressure, the vacuum system uses a fine leak valve to control the pumping rate. This assures that the initial pumping does not eject a levitated particle as gas is pumped out behind the slide mechanism. Once the system is pumped down to high vacuum, the fine leak valve is closed to allow separation of the vacuum pump from the chamber. A getter pump helped maintain vacuum in the chamber after the turbopump was detached. Finally, a thermocouple gauge installed at the chamber's vacuum port provided a monitor for pressure in the chamber between 0.1 mtorr and atmospheric pressure.

[12]Vacuum chamber built by Kimball Physics, Inc., Wilton, NH

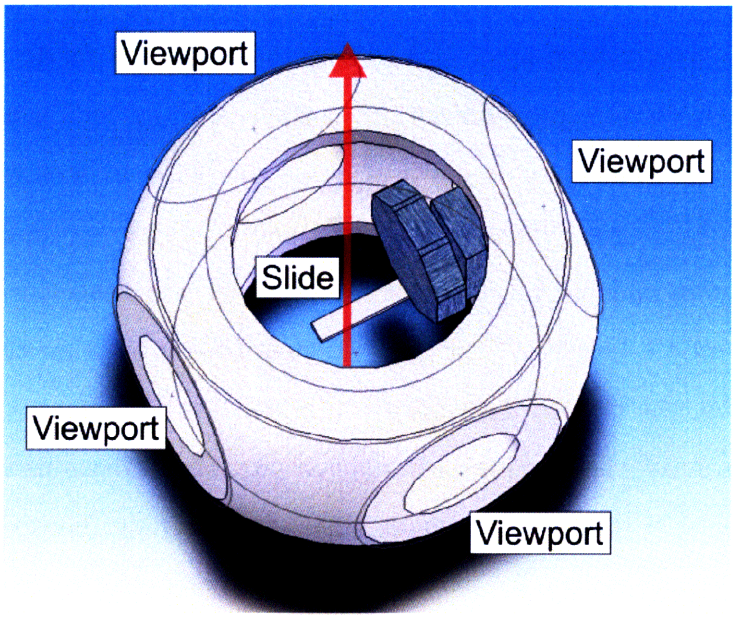

Figure 4-4: Design of the vacuum chamber that houses the particle launching slide and provides optical access for the levitating beam and detectors.

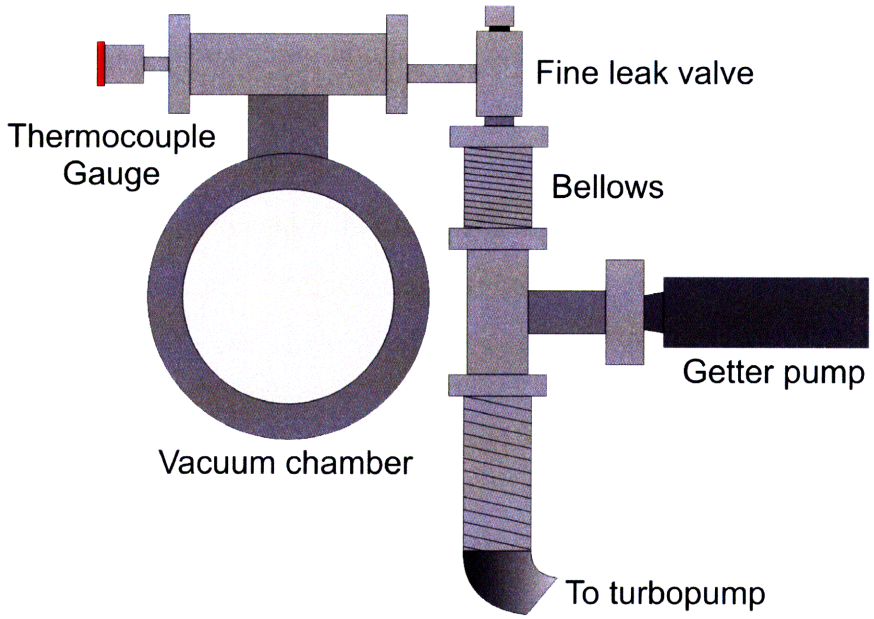

Figure 4-5: Diagram of the vacuum system. A turbopump is used for roughing and a getter pump is used for pumping down to high vacuum.

4.7 Optical force rebalancing loop

While a levitated particle in a single beam is stable at atmospheric pressure, the loss of viscous drag at high vacuum destabilizes the particle without feedback stabilization. As a result, the decay time of particle oscillations along the beam axis increases as the pressure decreases; at the limit of zero viscous damping, the only intrinsic damping mechanism is a Doppler-like change in incident intensity on the particle. The reflective force exerted by the laser beam changes by a factor of $(1 \pm v/c)^2$, depending on whether the particle is moving toward or away from the beam with velocity v (relative to the beam optics). For a particle levitated against gravity, the damping constant of particle oscillations is $\approx 2g/c$ (equivalent to a time constant of $\approx$ 0.7 years) [Ash76]. Intrinsic damping, however, does not become dominant until pressures below 10^{-9} torr (for a 10 μm particle)[13]. Feedback stabilization, therefore, is not only needed to measure acceleration, but to keep a microsphere trapped in high vacuum.

4.7.1 Particle position detection

To measure particle position along the laser beam axis, reflected light from a levitated microsphere (refer to figure 3-2) is focused with a microscope onto a split photodetector over a 30 cm distance. Figure 4-6 shows the optical design of this system. Resolution of the particle position increases with this distance, so it is a key design factor for developing a sensor. The split photodetector measures the sum of light on the detector and the difference between the light detected on the top and bottom halves[14]. The normalized difference signal, which is proportional to particle displacement from the center of the detector, is directed to a digital controller as an error signal.

4.7.2 Feedback control

After detecting the particle position, a National Instruments PXI Real-Time data acquisition system reads the normalized difference signal from the split photodetector. A digital PID controller, shown in figure 4-7, was programmed in National Instruments LabView 8.5 to

[13]This is one of the lowest-loss mechanical oscillators ever realized.
[14]New Focus Quadcell Photoreceiver Model 2901 (Si)

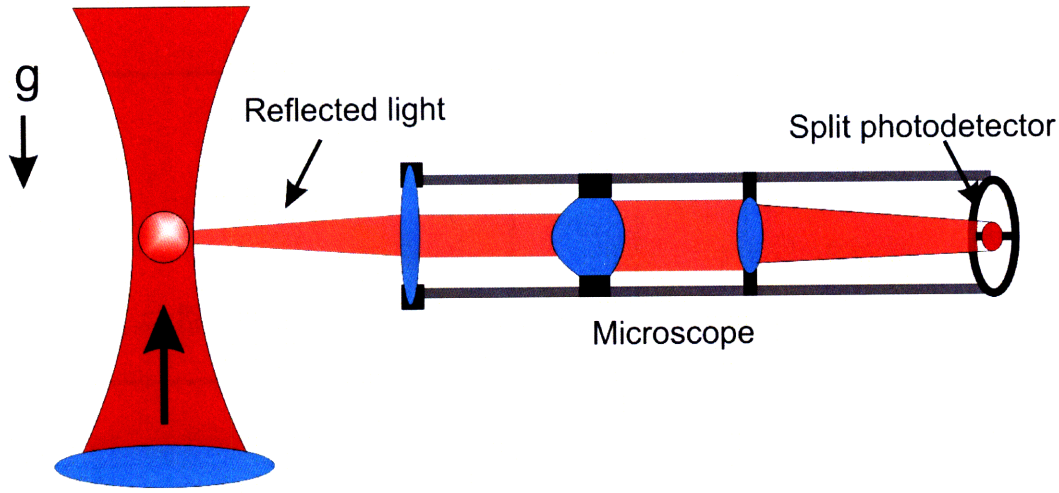

Figure 4-6: Diagram of the particle position detector.

tune a fast variable optical attenuator (see appendix B for code)[15]. The optical attenuator, in turn, adjusts the levitating beam power to control particle position. The PID loop was tuned to critically damp particle position displacements, and updated the optical attenuator at 200-300 Hz.

4.7.3 Fast variable optical attenuators

A fast variable optical attenuator (FVOA) controlled the levitating beam power. As motivated in section 4.3, FVOAs achieve faster and lower noise optical power control than direct modulation of laser current. In the current apparatus, these devices limit the bandwidth of the rebalancing loop, depending on the time required to adjust the internal attenuation mechanism (e.g., a grating).

Two types of inline fiber FVOA devices are commercially available and are capable of sub-millisecond response times. MEMS FVOAs selectively reflect input light with an actuated grating and direct it out through an output fiber[16]. Solid state FVOAs are even higher performance systems, and are capable of < 500 ns rise times[17]. These devices utilize optical properties of organic crystals. Some experiments were done with a custom solid state FVOA

[15]PID stands for Proportional-Integral-Derivative control. The transfer function of a PID loop from the error signal $E(s)$ to the controller output $U(s)$ is: $U/E = k_P + k_D s + \frac{k_I}{s}$, where k_P, k_I, and k_D are the proportional, integral, and derivative gains.

[16]DiCon FiberOptics, Inc., Richmond, CA.

[17]The rise time of an FVOA is the time required to fully attenuate the input light from zero attenuation.

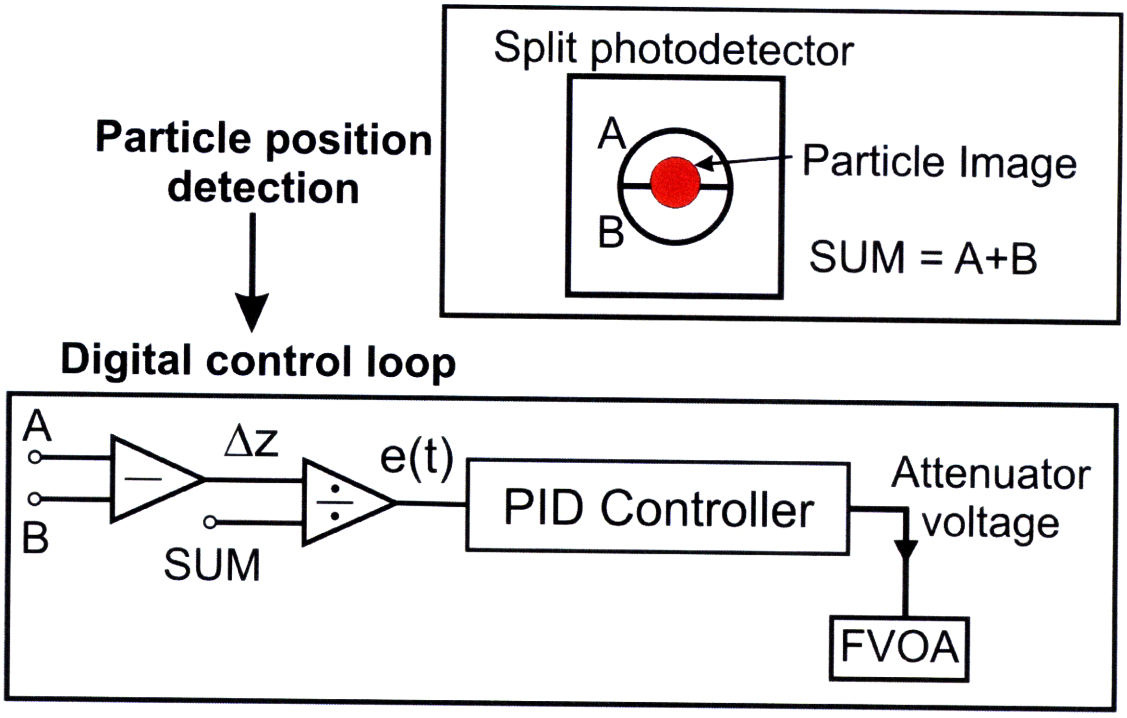

Figure 4-7: Diagram of the digital control loop and the source of the error signal $e(t)$.

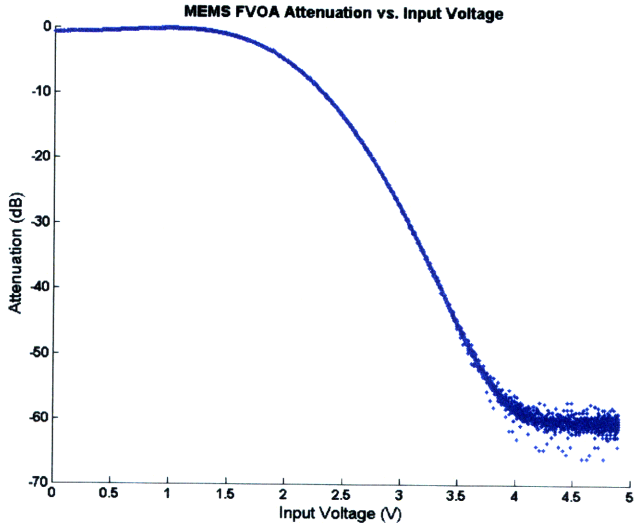

Figure 4-8: Input-output attenuation of a laser beam by a MEMS FVOA (made by DiCon FiberOptics, Inc.).

built by Agiltron[18]. Both MEMS and solid state FVOAs are low power, compact devices (the DiCon MEMS attenuator uses $< 20\mu$W), and will serve well in a compact, deployable sensor. The table below summarizes the performance of these two optical attenuators.

Specification	MEMS	Solid State
Attenuation Range (dB)	0 - 55	0 - 40
Slope (dB/V)	20 (max.)	10 (ave.), 90 (max.)
Response Time	1 ms	200 ns
Dimensions	5 mm (diam) x 40 mm	6 (diam) x 65mm

Table 4.2: Specifications of MEMS and solid state FVOAs used in experiments.

4.8 Summary

The next chapter discusses the results of experiments with the apparatus described here. Suggestions for future modifications to the current apparatus are included in chapter 6.

[18]Agiltron, Inc., Woburn, MA. Nanospeed FVOA customized for 1064 nm

THIS PAGE INTENTIONALLY LEFT BLANK

Chapter 5

Preliminary Experimental Results and Performance Diagnostics

The goal of this thesis was to design and build the first light force accelerometer which could levitate glass microspheres in high vacuum and demonstrate optical force rebalancing. The apparatus described in the previous chapter achieved these important capabilities, permitting tests of its sensitivity and bias stability for a 1 g input.

Since the current vertically-oriented single beam apparatus can only measure acceleration about a constant 1 g input, the most meaningful performance metrics are short term sensitivity and bias stability. Therefore, all experiments in this work were static tests. Full characterization of the accelerometer performance involves multi-position tests in which parameters like scale factor, cross-axial coupling and fixed biases (biases occurring when there is no input along the accelerometer's sensitive axis) can be measured. For the LFA, multi-position tests require a two-beam system in which a particle is trapped by two counter-propagating beams (as shown in figure 3-4). Nevertheless, experiments with the current single beam apparatus served to identify elements of the system that are currently limiting it from achieving higher sensitivity and short term bias stability. A description of recommended future work with the system is included and summarized in chapter 6. The results presented in this chapter include:

- Demonstration of levitation and optical force rebalancing in high vacuum
- Verification of photophoretic force effects for varying pressure

- Preliminary accelerometer performance tests for 1 g input
  - Short term sensitivity
  - Bias stability
  - Analysis of factors limiting performance

5.1 Demonstration of particle levitation in high vacuum

As described in chapter 3, the LFA will achieve higher sensitivity when the levitated proof mass is in high vacuum. Gas molecule collisions with the proof mass result in degraded short term sensitivity as it is randomly perturbed. For a free aerosol particle in a gas, these frequent collisions result in a random walk (Brownian motion). Trapping the particle in a laser beam prevents a random walk from occurring, but does not eliminate particle jitter.

In high vacuum, these effects are minimized because the mean free path of the gas molecules is longer, so the average time between collisions with the levitated proof mass increases correspondingly. Levitating a particle at low pressures, however, becomes challenging because of the loss of viscous damping forces on the particle. In the current apparatus, glass microspheres with a 10 μm diameter were launched and trapped in a vertically-pointed laser beam of 65-75 mW. Figure 5-1 shows an image of a levitated borosilicate glass sphere over the glass slide it was launched from. As previously mentioned, launching particles into the laser beam at atmospheric pressure is easier than launching in vacuum because particles leave the slide with high velocities and escape the beam without trapping. In air, viscous damping slows particles and increases the likelihood of being captured by the beam. In all experiments, particles were never both launched and trapped below $\approx$ 1 torr.

5.1.1 Limitations of particle levitation in high vacuum

Once a particle is levitated at atmospheric pressure, the vacuum chamber can be evacuated. As the chamber pressure decreases, it was observed that more absorptive particles require significantly more applied optical power to maintain a fixed position. For borosilicate glass

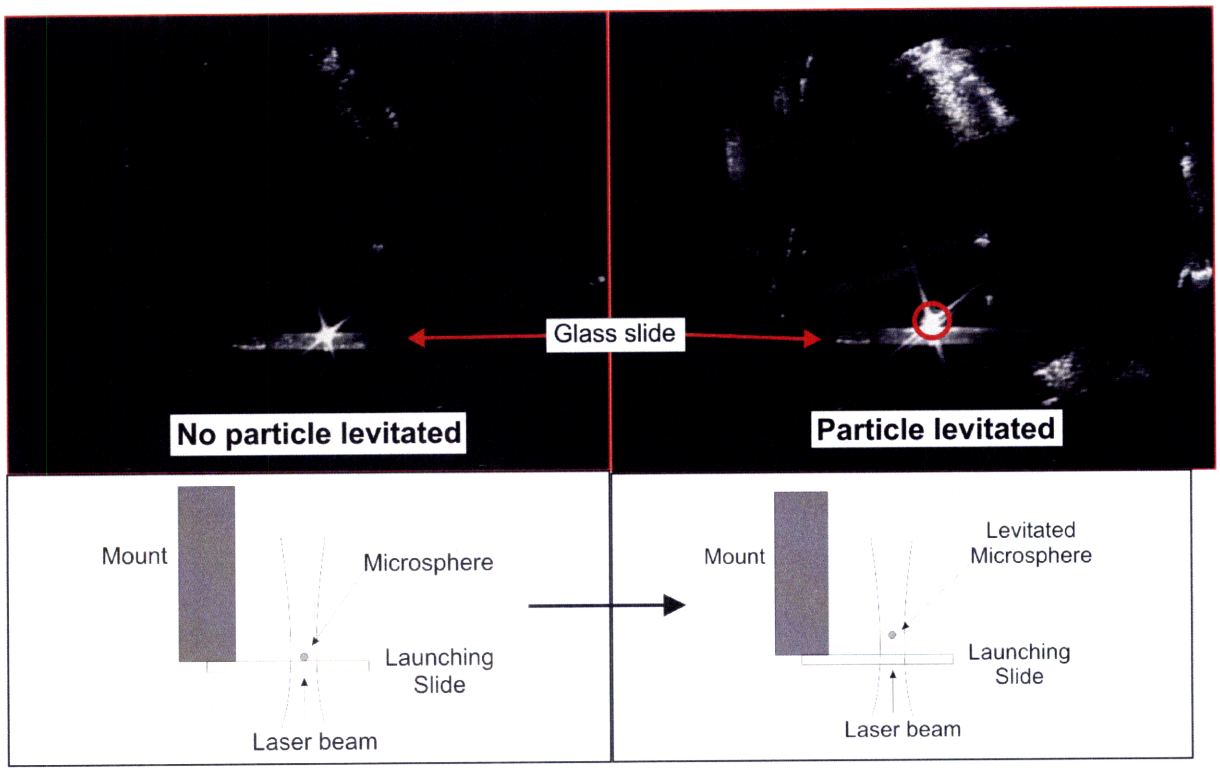

Figure 5-1: A 10 μm borosilicate glass particle (circled on right) levitated by a 75 mW laser beam in the vacuum chamber. Image on the left shows chamber before particle was launched for comparison. Notice how the levitated particle illuminates the chamber with scattered light.

microspheres, levitation at pressures around 1-10 torr required as much as 40% more light than the amount required to levitate them at atmospheric pressure. This added downward force, which decreases at pressures higher and lower than this pressure range, is best explained by photophoretic effects. As predicted by the photophoresis analysis in section 2.3, negative photophoresis (which produces a net force against the laser beam) should occur for 10 μm particles levitated by a laser beam with a 980 nm wavelength. This implies that photophoretic forces can be as large as 3-4 pN for a borosilicate microsphere that weighs about 10 pN. Therefore, changes in pressure will generate large biases if particles are levitated near this critical pressure range.

Levitation of borosilicate particles in high vacuum was prohibitively difficult because of the instability produced by photophoretic forces. Furthermore, once a particle remained trapped down to lower pressures and photophoretic forces abated, particle rotations frequently ensued and accelerated until the particle was ejected from the beam. In section 2.3.1 it was shown that angular momentum transfer from absorption of circularly polarized light applied a torque on a particle. In many experiments with these microspheres, visual observations of levitated particles revealed wobbling or vertical oscillations coupled to high frequency rotations (as high as 100 Hz). Manual polarization control of the levitating beam was used to compensate for these rotations, but this method was not consistently able to prevent rotations from occurring. Video taken when rotations occurred revealed that surface irregularities or the presence of contaminants (e.g., dust) which reflect more or less light than the glass are sources of instability. In each of these cases, the force imparted by a laser beam would be asymmetric or non-uniform, and could lead to rotation or more chaotic motions. This motion was visible by observing light scattered from a levitated microsphere on the inner surface of the vacuum chamber. Distinct features of the particle surface were projected on the vacuum chamber, making rotations easily detectable. Measurements of light reflected by a rotating particle onto a photodiode also exhibited high frequency oscillations, supporting this explanation. Ultimately, use of more spherical fused silica microspheres reduced these effects.

5.1.2 Levitation of synthetic fused silica microspheres

To reduce the effects of photophoretic forces, purer fused silica microspheres were fabricated in the lab. Typical silica glass has an absorption coefficient $\approx$ 400 times smaller than borosilicate glass at a wavelength of 1 μm; since photophoretic effects are proportional to the amount of absorbed light, these forces should be reduced in magnitude by a comparable factor. Samples of pulverized fused silica were made and injected via a gas line into the flame of an oxyhydrogen torch, where the glass particles heated and fused[1]. In fusing, surface tension formed spherical particles before they were quenched and cooled in a bath of distilled water[2]. An oxyhydrogen torch was selected instead of the more common oxy-acetylene torch because the flame of an oxyhydrogen torch is cleaner. The only chemical product of the flame is water, rather than an organic compound which could lead to surface contamination. Particles with diameters of 10-15 μm were selected with multiple stages of precise electroformed sieves[3].

These in-house fabricated silica particles were consistently levitated with the same optical system, and were easily trapped down to below 10 torr, where photophoretic force peaks. The downward force observed with borosilicate particles was not observed with these purer microspheres. Unfortunately, particle rotations still prevented long duration levitation in higher vacuum. The persistence of rotations in these low loss microspheres further indicates that surface irregularities are the underlying cause of these perturbations.

Long term levitation was finally achieved with fused silica microspheres made by Corpuscular, Inc., which were consistently more spherical. With a free-running laser, these spheres were trapped down to 10^{-4} torr without feedback stabilization for periods as long as 5-6 hours, when structural vibrations led to ejection of the sphere. With the application of rebalancing, trapping for almost indefinite periods was achieved. Trapping at lower pressures was limited only by the vacuum system.

[1]Made with samples of Corning HPFS Fused Silica 7980.

[2]An acknowledgment is made to Arthur Ashkin, who proposed this method in private communication [Ash07].

[3]Precision steel electroformed sieves were made by Gilson Company, Inc.

5.2 Demonstration of optical force rebalancing

The current apparatus also demonstrated the capability of optical force rebalancing, which will be used in a complete LFA to measure acceleration. The first step in proving this capability involved controlling particle position along the beam axis. Using the particle position detector described in section 4.7, reflected light from levitating particles was focused onto the center of a split photodetector. This alignment provided a set point for the feedback loop to measure particle position against. The power of the particle image on the detector was measured at 10-15 μW, with a FWHM beam width of $\approx$150 μm. A beam profiler was used to focus the image before centering on the detector.

As described in section 4.7.2, the feedback loop used the normalized difference signal from the detector, or the difference between the photodiode signals of the top and bottom halves of the detector divided by their sum) as the error signal. This error signal was sampled by the digital PID loop described in section 4.7.2 (code is in appendix B). Since little viscous damping occurs at low pressures, proportional control alone (effectively creating a mass-spring system) would lead to persistent oscillations. To compensate for a particle's velocity, derivative control (applies feedback proportional to the derivative of the error signal) must be used in adjusting the beam power.

A standard experiment for testing the performance of a feedback control system involves applying a sudden bias to the error signal and analyzing the response of the system as it tracks the new set point. In the apparatus, this was achieved by adding a bias to the normalized difference signal from the split photodetector. As shown in figure 5-2, this bias forces the optical rebalancing loop to apply more or less power to shift the image of the particle up or down on the detector, such that the difference in signals from the top and bottom halves (V_A and V_B, respectively) is zero. Measuring the step response is a useful tool for tuning the digital controller gains, and allows one to tune the loop for critical damping.

The results of one of these experiments are shown in figure 5-3. The response has no overshoot and achieves a rise time of < 75 ms for a change in position of 50 μm, thus achieving near critical damping. The response of the particle to a step input was also visible in video observations of the experiment. An alternative method to test optical rebalancing is to mechanically change the set point. By placing the split photodetector on a translation

stage, changes in the detector height forced the particle to track its motion (the particle image then remained centered on the detector).

The primary importance of these tests is in ensuring that the apparatus can measure acceleration. As long as the rebalancing loop nulls particle displacements measured on the split photodetector, changes in the levitating beam power provide a measurement of acceleration. Once optical rebalancing was demonstrated, the sensitivity of the apparatus could be tested.

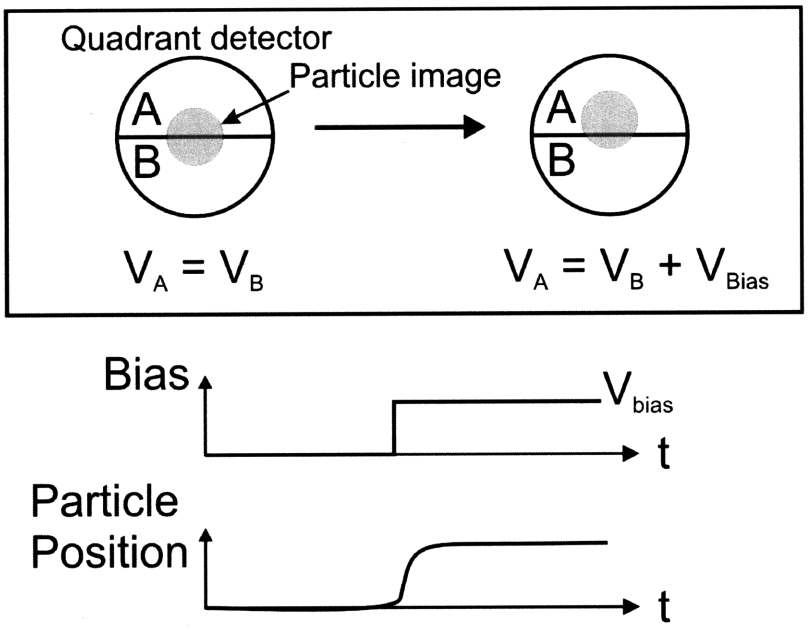

Figure 5-2: Step response of a levitated particle when optical rebalancing is active and a bias is applied to the feedback loop error signal.

5.2.1 Short term sensitivity

The short term sensitivity of an accelerometer is a measure of the instrument's ability to detect small accelerations over short time intervals, when longer term drifts or biases are negligible. For this apparatus, sensitivity was determined by sampling a portion of the levitating beam power (this beam will be called the measurement beam, as shown in figure 4-1) at 1-2 kHz for several minutes. This sampling rate was chosen to capture the controlled power adjustment made by the rebalancing loop, which was run at 200-300 Hz.

Figure 5-4 shows the accelerometer output over a 10 second period. The sensitivity was

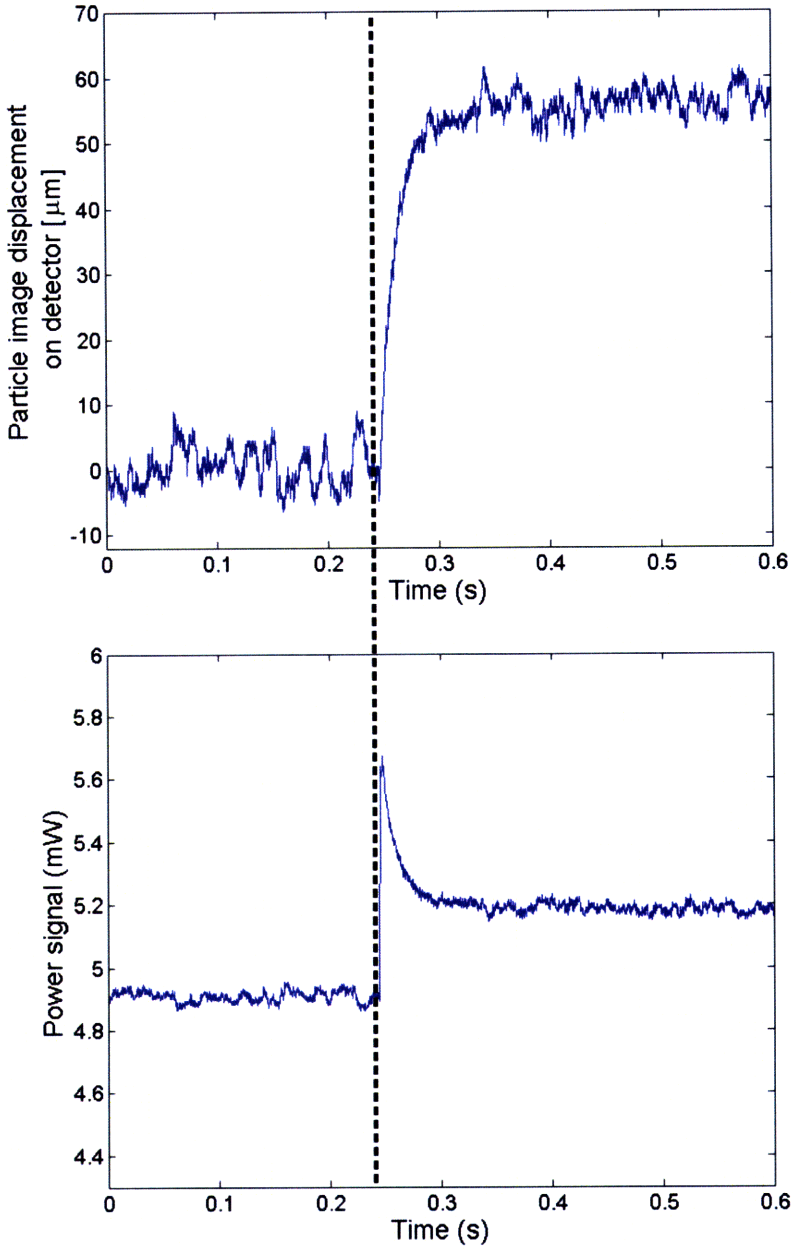

Figure 5-3: Response of the particle to a step change in bias on the split photodetector error signal.

calculated from one minute of data as the fractional uncertainty in the measurement of steady-state beam power (corresponding to levitating the microsphere at 1 g). The sensitivity, Δa, is therefore

$$\frac{\Delta a}{g} = \frac{\sigma_P}{\langle P \rangle} = \mathrm{SNR}^{-1} \tag{5.1}$$

where σ_P is the standard deviation of the measurement beam signal, $\langle P \rangle$ is the mean power over this time period, and SNR is the signal-to-noise ratio. From these data, the signal-to-noise was calculated to be 265, corresponding to a normalized short term sensitivity of Δa = g/(265 $\sqrt{1\mathrm{kHz}}$) = 119 $\mu g/\mathrm{Hz}^{1/2}$. A Fourier transform of the measurement beam signal in figure 5-5, however, shows that lower sensitivity would be obtained at lower frequencies (< 100 Hz) where larger non-white noise dominates. The sensitivity at frequencies around 1 Hz is 1-3 m$g/\mathrm{Hz}^{1/2}$.

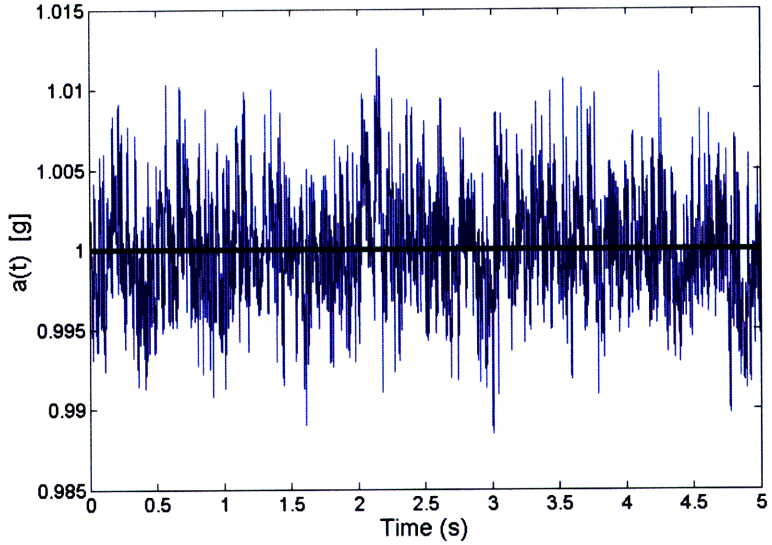

Figure 5-4: Accelerometer output under constant 1 g input. The short term sensitivity was calculated to be 119 $\mu g/\mathrm{Hz}^{1/2}$.

Two major error sources were identified by these data. A Fourier transform of the measurement beam signal revealed laser intensity noise as a significant noise source in providing a peak noise of about 20-30 $\mu\mathrm{g}/\mathrm{Hz}^{1/2}$ at 520 Hz and a white noise background of 1 $\mu\mathrm{g}/\mathrm{Hz}^{1/2}$. The laser stability was independently measured as 0.1% in one second, which corresponds to 30 $\mu\mathrm{g}/\mathrm{Hz}^{1/2}$ of noise. The most significant error source, however, is particle position measurement.

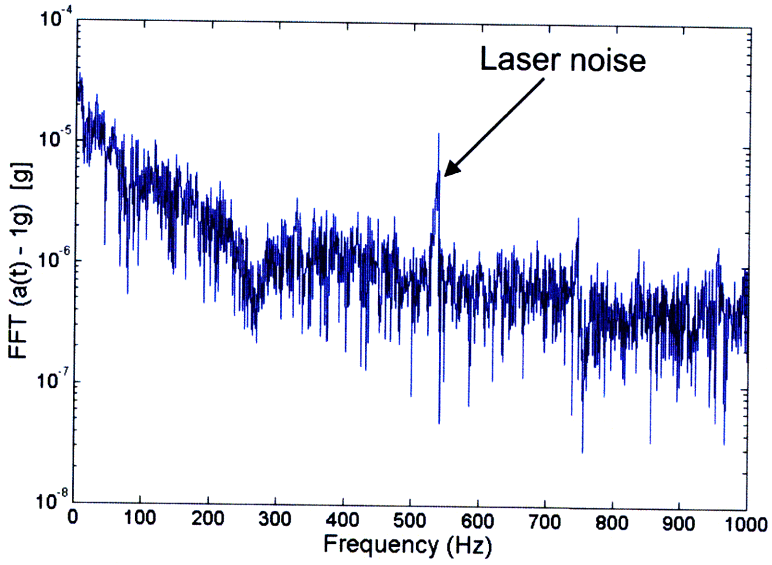

Figure 5-5: Discrete Fourier transform of the accelerometer output minus a 1 g offset.

5.2.2 Particle position resolution

In a force feedback accelerometer, the resolution of proof mass displacements, either by a mechanical transducer or by the particle position detector in this system, inherently limits its sensitivity. For instance, if an accelerometer can only distinguish proof mass displacement Δx during a measurement interval t, a constant acceleration of $\Delta a \approx (2\Delta x)/t^2$ could not be resolved.

For the LFA, the fundamental limit on position resolution is due to shot noise-limited measurement of the reflected particle image on a split photodetector. For a particle image of width $w_\circ$, mean photon counts per second $\langle N \rangle$, and standard deviation of photon counts per second σ, the position resolution δx is

$$\frac{\delta x}{w_\circ} \approx \frac{\sigma}{< N >} = \frac{1}{\sqrt{< N >}} \tag{5.2}$$

In experiments with the current apparatus, the particle image focused on the detector is about 15 μW. The shot noise limit for position resolution on a 150 μm-wide beam with this power is $\approx 10^{-11}$ m/Hz$^{1/2}$.

With the current particle position detector, position resolution was measured by adding a small amplitude sinusoidal power variation at frequency f to the steady-state levitation

power, as shown in figure 5-6. For small amplitudes, the particle responds as a linear second-order system (allowing one to neglect variations in beam intensity over a small range of position in the beam). The expected particle oscillation amplitude Δx is related to the amplitude of power variation ΔP by

$$\frac{\delta a}{g} = \frac{\omega_\circ^2 \Delta x}{g} = \frac{\Delta P}{P} \tag{5.3}$$

where $\omega_\circ = 2\pi f$ and Δa is the maximum acceleration the particle undergoes for an extra sinusoidal power input. Thus, the particle oscillation amplitude is

$$\Delta x = \frac{g \Delta P}{\omega_\circ^2 P} \tag{5.4}$$

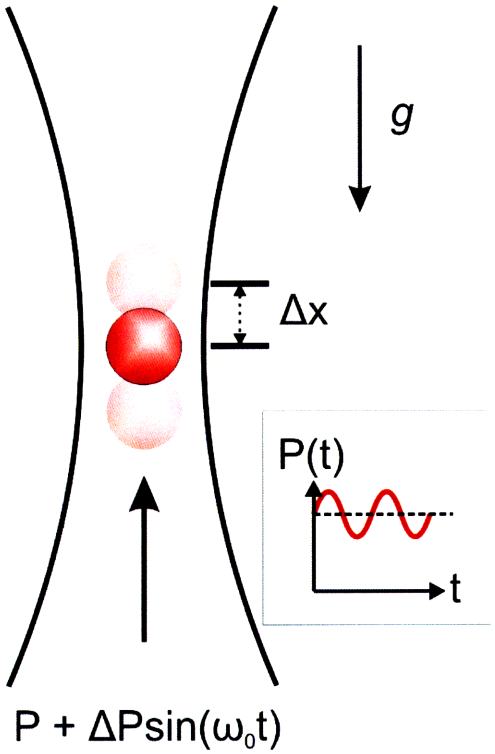

Figure 5-6: Diagram of position resolution experiment.

To determine the ultimate resolution of the particle position detector in the current system, a 10% power variation was introduced at $f = 10$ Hz while a particle was levitated without feedback stabilization (open loop). This corresponds to an oscillation amplitude of $\Delta x = 250$ μm. Figure 5-7 shows the particle response measured on the split photodetector.

From a Fourier transform of the oscillating position signal, the signal-to-noise for resolving a 250 μm oscillation amplitude is 30. This indicates that the system should be able to resolve particle position to about 8 μm in one second. Since this position was measured against a white noise background, this should improve as $t^{-1/2}$. The position resolution is then 8 $\mu m/Hz^{1/2}$ (about one particle diameter in one second). For lower oscillation frequencies (< 5 Hz), the Fourier transform in figure 5-7 shows that a lower signal-to-noise would be obtained, given that the noise background is higher below this frequency.

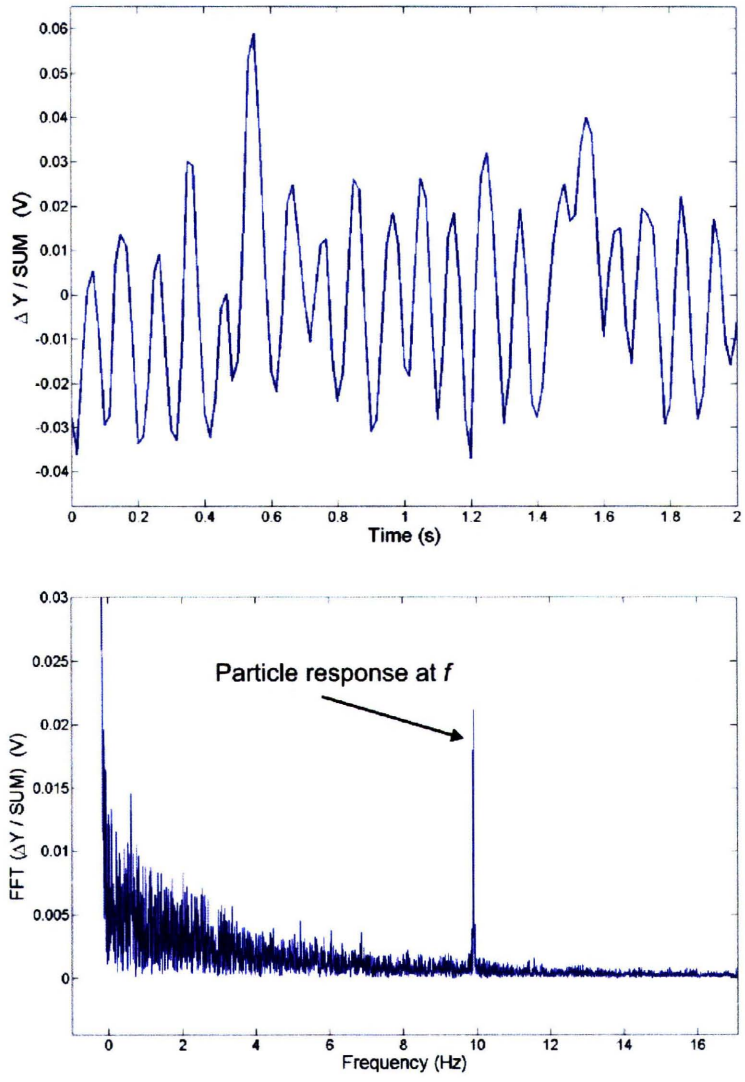

Figure 5-7: Top: The split photodetector normalized difference signal measuring particle oscillations from a sinusoidal power input at 10 Hz (the signal can be calibrated to particle position by the factor 80 $\mu V/\mu m$). Bottom: Discrete Fourier transform of the particle position signal with a peak at the oscillation frequency f.

Over longer data sets, however, the position signal exhibits short term jumps which are measured as acceleration. Figure 5-8 shows two of these features detected while the system was in open loop (no power adjustments). These sudden displacements indicate accelerations of as much as 400 μg, even though the laser power was stable to within 0.01%, which corresponds to a levitating force stability of < 100 μg for the duration of these jumps. Based on video observations of light scattered by the particle onto the vacuum chamber walls, these drifts correspond to visible changes in the orientation of the particle (e.g., rotations or wobbles). This effect will become important in an assessment of the bias stability of the apparatus.

5.3 Long term stability

To determine long term stability of the LFA, measurements of constant 1 g acceleration were taken for several hours. In all data sets taken with the apparatus, linearly increasing trends in the required levitation power for a constant 1 g input were observed for several hours after sealing the vacuum chamber. Figure 5-9 shows such a drift over a 2 hour data set. Similar increases in power were measured in other long term data sets. These slow, linear drifts were accounted for by measured increases in the chamber pressure. Since a vacuum pressure of only 10^{-4} torr was achieved, photophoretic forces are still present[4]. During these 2-3 hour runs, the pressure increased linearly to 10^{-3} torr. The increase in photophoretic force against the laser beam for this change in pressure is approximately 10 (refer to figure 2-5). The magnitude of photophoretic force for fused silica is a factor of 400 smaller than for borosilicate glass (given by the ratio of the absorption coefficients). For a measured pressure change from 10^{-4} torr to 10^{-3} torr, the photophoretic force should accelerate the particle downward by $\approx 0.01g$. The data in figure 5-9 show a comparable increase in the levitating beam power to compensate for this extra force. With this systematic drift accounted for, it may be subtracted so inherent bias stability analysis can be made below.

[4]Limited vacuum was achieved because it was impractical to bake out the chamber, given that it was frequently opened for depositing new particles on the launching slide. Several outgassing sources in the chamber also contributed to protracted pumping time.

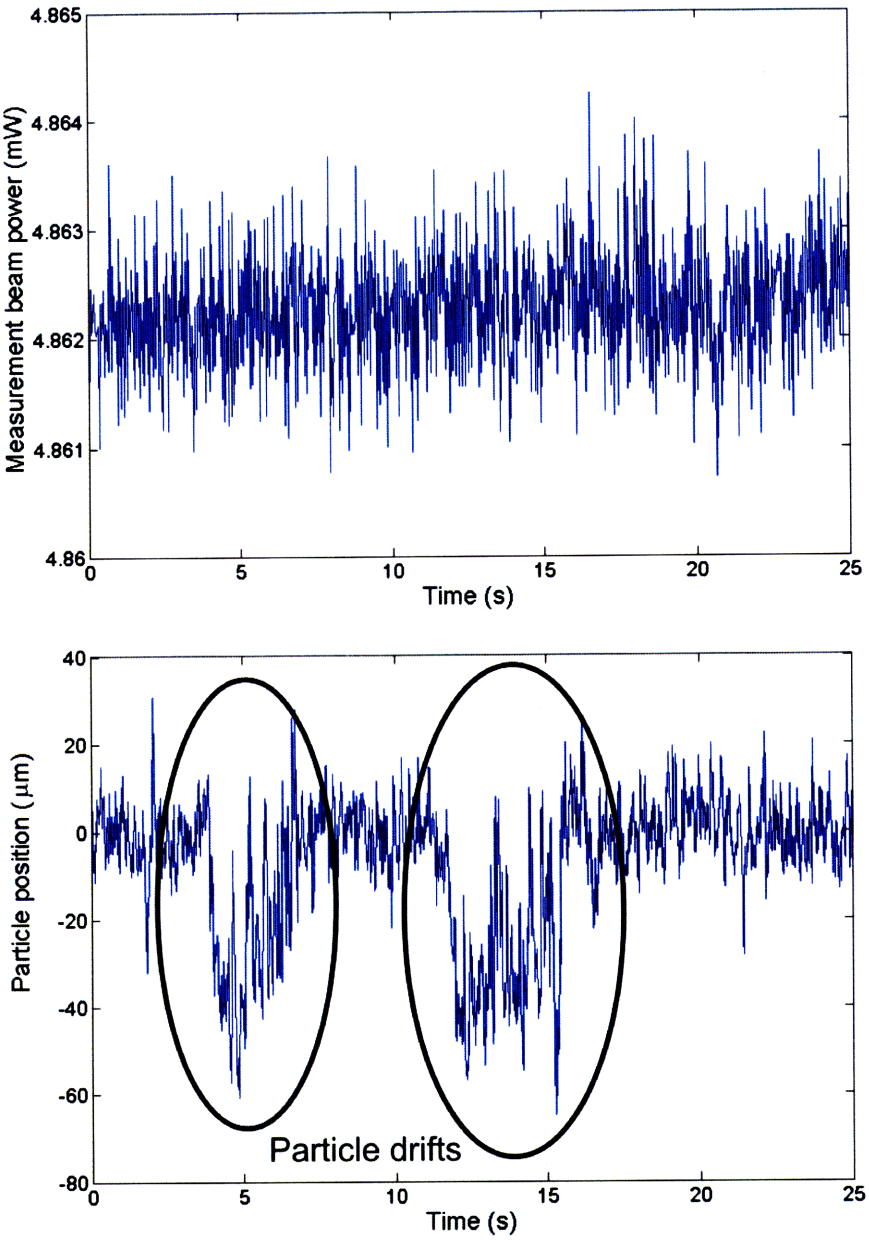

Figure 5-8: Example of measured particle shifts which are due to particle surface irregularities.

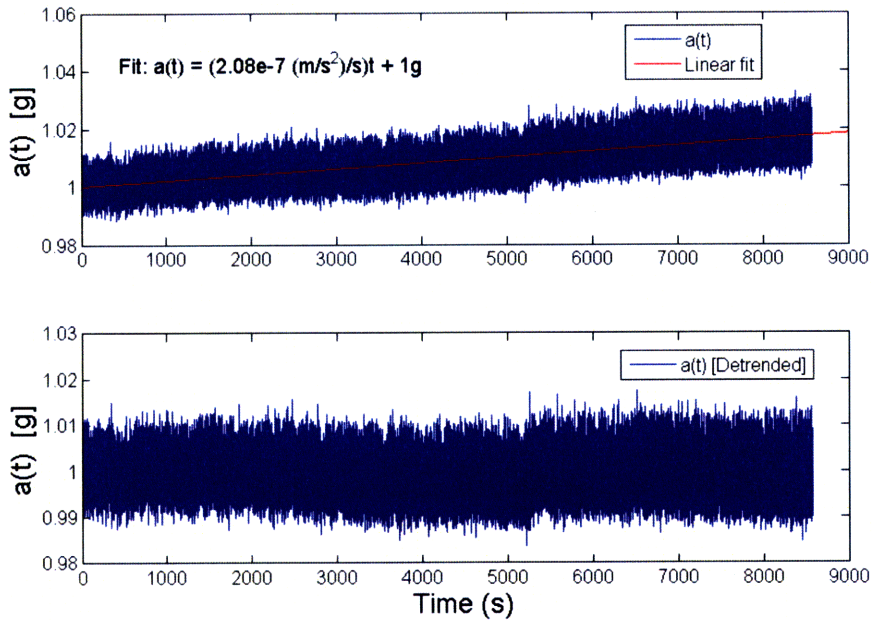

Figure 5-9: Accelerometer output over a 2.2 hour period. The trend in the top plot can be accounted for by photophoretic forces.

5.4 Bias Stability

The bias stability of the apparatus was tested by monitoring a portion of the levitating beam (the measurement beam) for periods of several hours while the rebalancing loop was active. To analyze the stability of the signal, the Allan variance was computed. This statistical measure is used because the standard deviation does not converge for most signals with drifts (e.g., random walks). The Allan deviation (the square root of the Allan variance) is calculated by binning a time-domain signal into constant measurement intervals, as shown in figure 5-10, and computing the standard deviation of the means of neighboring intervals. For a time series of acceleration measurements, the Allan variance $\sigma_y^2(\tau)$ for measurement interval τ is

$$\sigma_y^2(\tau) = \frac{1}{2(n-1)} \sum_i (a(t)_{i+1} - a(t)_i)^2 \tag{5.5}$$

where n is the number of bins and $a(t)_i$ is the mean of the ith bin[5].

The measurement beam was sampled at 1 kHz and 30 Hz for computing the Allan deviation at measurement intervals between 0.01 and 1000 seconds. Figure 5-11 shows Allan

[5]The Allan variance was developed historically for analyzing high precision clock stability.

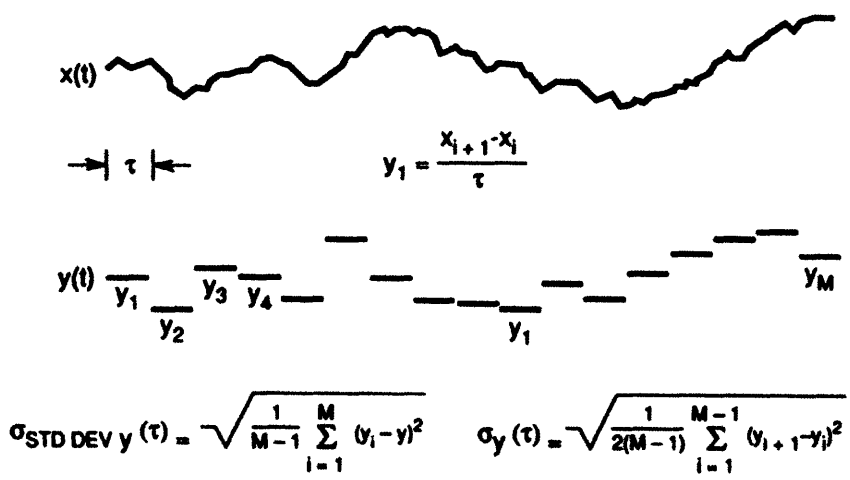

Figure 5-10: Method for computing the Allan deviation of a time-domain signal. Adapted and reprinted with permission from [NST08].

deviations for this range of intervals. Allan deviations for longer measurement intervals (> 1 s) were computed from linear drift-subtracted data (accounting for the linear drifts observed in long data sets due to increasing photophoretic forces, as seen in figure 5-9).

For measurement intervals less than one second, the Allan deviation remains nearly constant, indicating bias instability for measurement intervals up to 1 second. As discussed in section 5.2.2, particle position drifts caused by surface irregularities is the cause of short term bias instability. It is only for measurement intervals greater than 30 seconds that these biases begin to decrease as $\tau^{-1/2}$.

Bias stability is conventionally quoted as the minimum of the Allan deviation plot. Although the Allan deviation minimum is at longer measurement intervals than represented in these data, the best estimate of the bias stability of the current system is $< 250\mu g$. With a more efficient vacuum system, longer data sets can be taken to find the minimum of the Allan deviation curve.

In summary, the elements of the apparatus limiting sensitivity and bias stability include

- Short term bias instability due to particle surface irregularities
- Variable photophoretic forces resulting from long term pressure changes in the vacuum chamber

Chapter 6 addresses potential improvements in the apparatus and outlines major goals

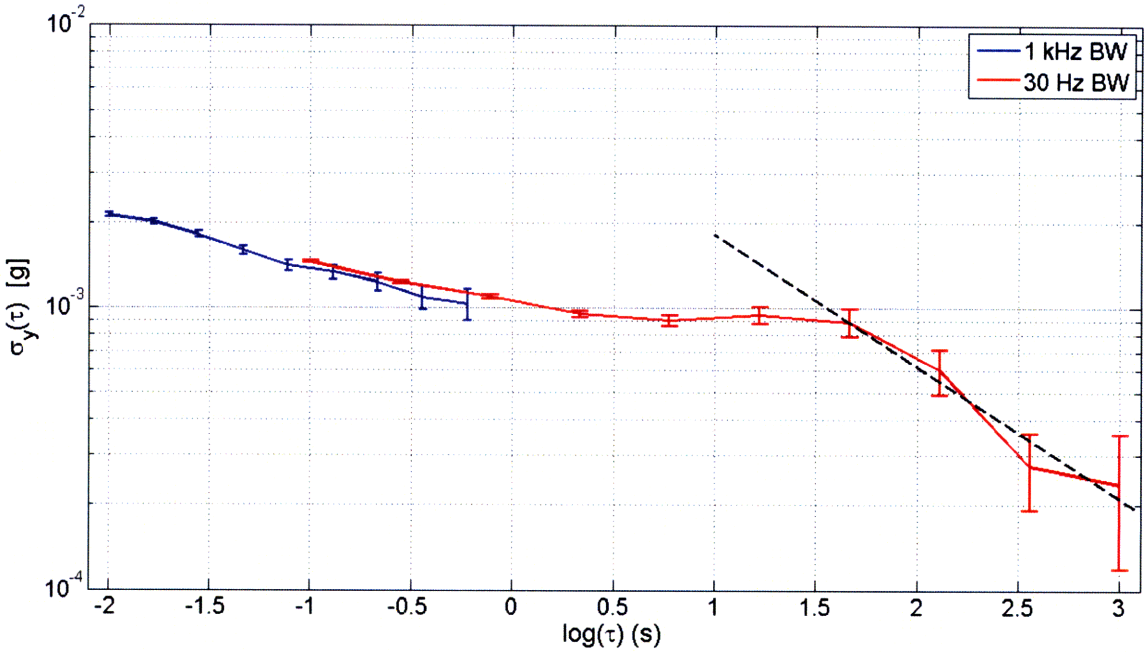

Figure 5-11: Allan deviations of LFA output for constant 1 g acceleration. The dashed line corresponds to a decrease in bias as $\sim \tau^{-1/2}$.

for future LFA development, including several applications.

THIS PAGE INTENTIONALLY LEFT BLANK

Chapter 6

Future Work

6.1 Conclusions

The results presented in this thesis demonstrate the feasibility of a light force accelerometer, and began to assess the performance of the instrument under a 1 g acceleration. The current implementation of the LFA is still far from reaching its estimated fundamental sensitivity limit of better than 100 $ng/\mathrm{Hz}^{1/2}$. The preliminary performance diagnostics presented in the previous chapter have revealed where the system is being limited in both sensitivity and bias stability. Important systematic factors affecting performance, including biases resulting from photophoretic forces and particle position detection, have been identified, and it is now worth considering how to improve upon the existing apparatus. This chapter discusses how future work can more completely characterize the performance of the LFA and expect to make improvements in sensitivity.

6.2 Goals for Future Work

The LFA can be advanced in several ways beyond achieving higher performance. More practical concerns such as reducing the time it takes to trap a particle could have a major impact on the suitability of the LFA for a deployable sensor. The elements of the current apparatus which could make the greatest impact on the operation and performance of the LFA include:

- Installation of a second, counter-propagating beam for operation in any orientation
- Development of efficient, reliable methods for launching and trapping particles
- Enhancing particle position detection

These goals will be discussed with some specific recommendations for modifying the current system or exploring a new approach.

6.3 Two-beam light force accelerometer

The most significant extension of the current system is the addition of a counter-propagating beam. As has been mentioned, this will not only permit complete accelerometer testing (measuring fixed biases, cross-axial coupling, determining scale factor and scale factor linearity), but also dramatically improve optical force rebalancing. With two beams, the system can apply force feedback to a trapped particle with significantly higher 'stiffness.' In the current single beam configuration, the LFA can only null vertical motion as fast as gravity can accelerate the particle downward.

The challenge in building a two-beam system will be achieving adequate beam alignment in a stable mounting. Fiber focusers on translation stages should accomplish this, and potentially create a very compact structure. With the use of fiber optic feedthroughs as shown in figure 6-1, these focusers could be installed in the existing vacuum chamber.

6.3.1 Particle launching

The current method for particle launching consistently traps particles in less than one minute, but it may not be suitable for launching in other orientations or in vacuum. Slide vibrations are also a source of biases, since it they deflect and distort the levitating beam before reaching the levitated particle. This can generate large particle oscillations in high vacuum. Particle launching is a potential limitation in developing a deployable sensor, and should become a central focus for development efforts when the accelerometer achieves higher performance.

A potential modification to the existing design would involve drilling 'pinholes' in the slide so the beam can pass through unobstructed. Such an aperture should be made close

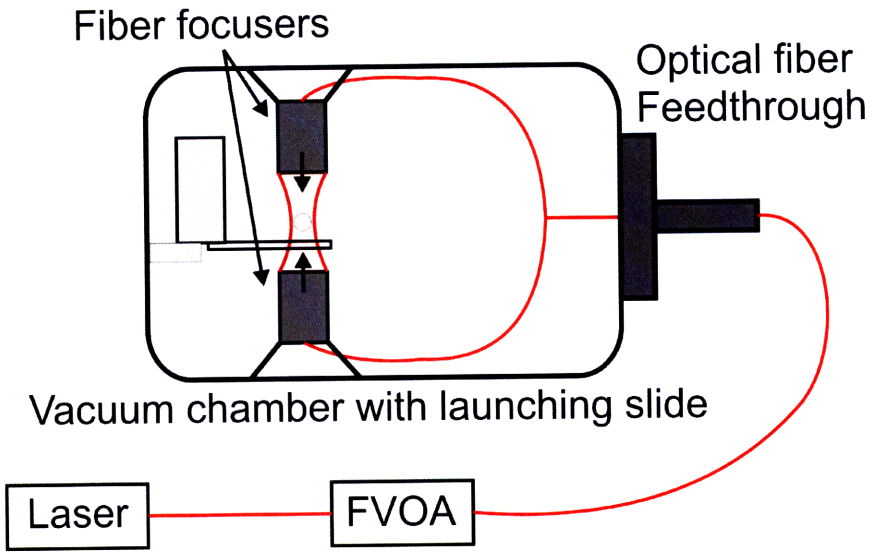

Figure 6-1: Diagram of a two-beam LFA using fiber focusers, the existing vacuum chamber and particle launching slide.

to a vibrational node, where particles are more likely to be launched from the slide. An opening of several hundred microns is sufficiently large to accommodate the beam and have little impact on the resonance structure of the slide.

The ultimate goal for advancing particle launching methods, however, is to be able to launch and trap in vacuum. This advancement would reduce the system's switch-on time and simplify the vacuum design of a sensor, since the system would not have to pump down for each particle launch.

6.4 Particle position detection

As discussed in chapter 5, short term sensitivity and bias stability are currently limited by particle position detection. Fabricating cleaner and more spherical particles would reduce this effect, but it is unrealistic to expect these results from current microsphere fabrication processes. One potential improvement involves illuminating the levitated microsphere with another laser beam. Figure 6-2 shows how a laser beam pointed perpendicularly to the trapping beams could produce a higher power signal on the quadrant detector. A different wavelength could be used in the illuminating beam to reduce sensitivity to light reflected from the levitating beams (the light which is currently used to detect particle position). For

instance, an indium gallium arsenide (InGaAs) detector could be used with an illuminating beam at 1550 nm, and would have negligible sensitivity to the 980 nm light used for trapping.

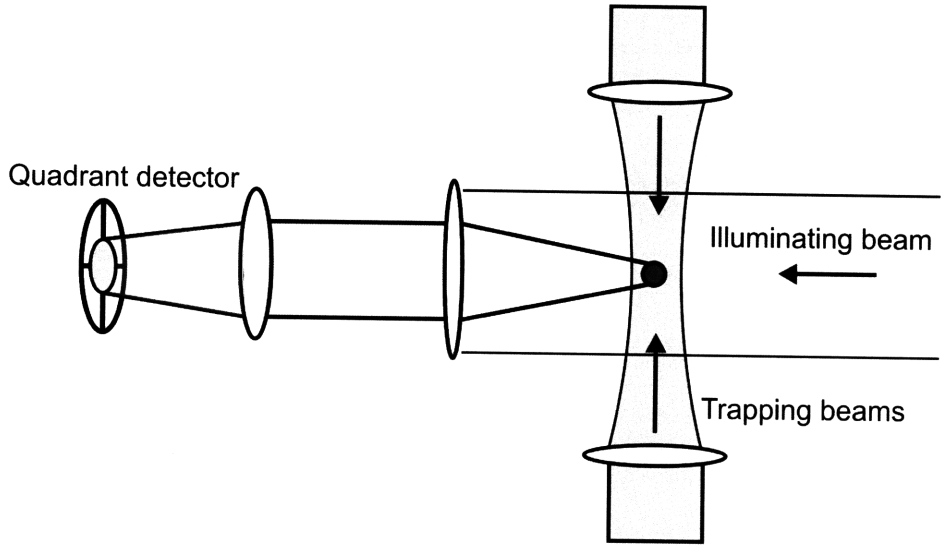

Figure 6-2: Diagram of an alternative particle position detection method involving an illuminating beam.

Of course, the illuminating beam will apply trapping forces to the particle as well, which leads to scale factor error (the rebalancing loop will not have to apply as much light to null particle motion). Cross-coupling may not be significant, however, because the illuminating beam power could be three to four orders of magnitude lower than the power of the levitating beams.

6.5 Applications

With these improvements made, a higher performance LFA could be developed for several interesting applications. In posing unique challenges for the LFA, more may be learned about the sensor's ultimate performance limits. For example, a high precision accelerometer with short-term sensitivity of $< 1 ng/\mathrm{Hz}^{1/2}$ is desired for gravimetry missions in which small deviations in the local gravitational field of an orbiting spacecraft are to be detected. In such a low inertial input situation, a LFA would be required to detect small proof mass displacements (<1 nm) in only seconds. A potential approach to these requirements is to trap

more massive microspheres with high power lasers, which would dramatically increase scale factor and make position measurement easier. Developing such an instrument would provide a test of the ultimate sensitivity of the LFA. It is hoped that the light force accelerometer will be developed for a range of demanding applications in the future.

THIS PAGE INTENTIONALLY LEFT BLANK

Appendix A

Calculation of momentum transfer to a spherical particle by a ray

This chapter details the calculation of the total force exerted by a ray of power P on a sphere at an angle θ from the normal, and is adapted from [Ash92]. Figure A-1 shows the subsequent partial reflections and transmissions which occur. A series of rays are scattered with powers $PR, PT^2, PT^2R, ..., PT^2R^n, ...$ The first reflected ray, with power PR, reflects at angle $\pi + 2\theta$ from the original ray. The second scattered ray leaves with power PT^2 at an angle α from the original ray. Subsequent scattered rays leave at angles $\alpha + \beta$, ..., $\alpha + n\beta$, ... The total forces in the z (axial) and r (radial) directions are calculated as the net change in momentum per second in each direction. The forces F_z and F_r are then

$$F_z = \frac{mP}{c} - \left[\frac{mPR}{c}\cos(\pi + 2\theta) + \sum_{n=0}^{\infty}\frac{mP}{c}T^2R^n\cos(\alpha + n\beta)\right] \tag{A.1}$$

$$F_r = 0 - \left[\frac{mPR}{c}\sin(\pi + 2\theta) - \sum_{n=0}^{\infty}\frac{mP}{c}T^2R^n\sin(\alpha + n\beta)\right] \tag{A.2}$$

$$\tag{A.3}$$

The factor $\frac{mP}{c}$ is the incident momentum per second in the original ray (initially all in the z direction). Finally, noting the geometric relations $\alpha = 2\theta - 2v$ and $\beta = \pi - 2v$ (θ and v are the angles of incidence and refraction of the ray, related by Snell's law), the infinite series in

each expression can be summed to

$$F_z = Q_z \frac{mP}{c} = \frac{mP}{c}\left(1 + R\cos(2\theta) - \frac{T^2[\cos(2\theta - 2v) + R\cos(2\theta)]}{1 + R^2 + 2R\cos(2v)}\right) \quad \text{(A.4)}$$

$$F_r = Q_r \frac{mP}{c} = \frac{mP}{c}\left(R\sin(2\theta) - \frac{T^2[\sin(2\theta - 2v) + R\sin(2\theta)]}{1 + R^2 + 2R\cos(2v)}\right) \quad \text{(A.5)}$$

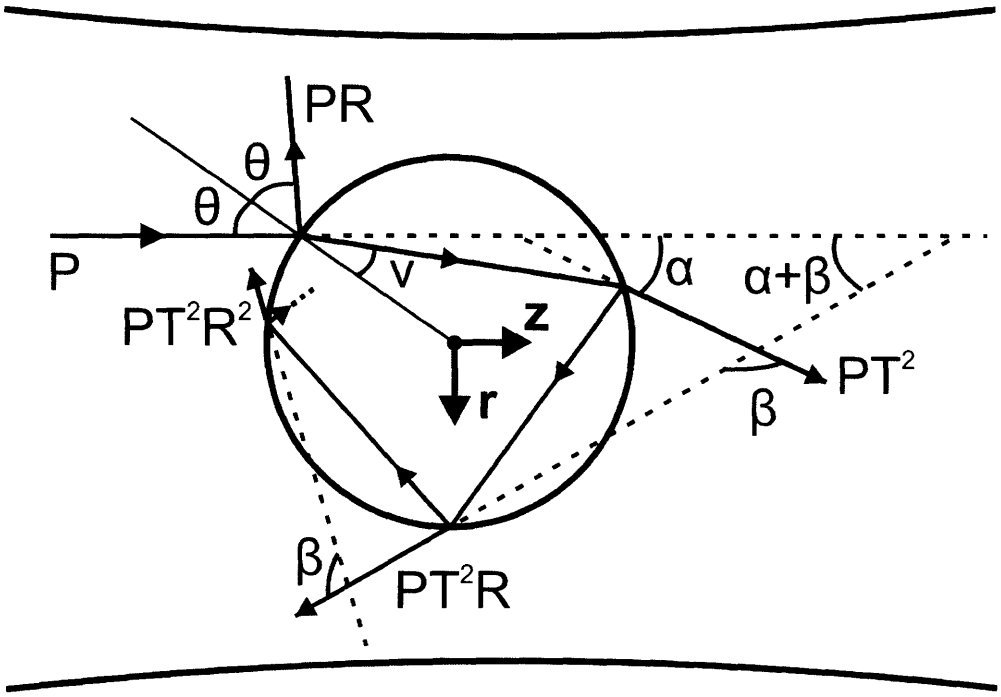

Figure A-1: Scattering of a ray by a spherical dielectric particle.

Appendix B

Optical Rebalancing Control Code

The code used to provide the input voltage to a fast variable optical attenuator (FVOA) for controlling the levitating beam is presented here for reference. It is essentially a discrete time PID loop, which samples an error signal, the normalized difference signal from a quadrant photodetector, and computes a voltage to apply to the FVOA to selectively attenuate the levitating beam. The control voltage sent to the FVOA over sampling interval dt for error $e(t)$ is:

$$u(t) - u_{Base} = K_P e(t) + K_I(e(t) - e(t - dt)dt + K_D \frac{(e(t) - e(t - dt)}{dt} \tag{B.1}$$

where the K_P, K_I, and K_D are the proportional, integral, and control gains and u_{Base} is the base attenuation. The base attenuation is whatever attenuation to the light coming from the laser source is fixed at to levitate the particle. Therefore, all control is computed relative to the power required to levitate the particle to the set point. This program was run on National Instruments LabView 8.5.

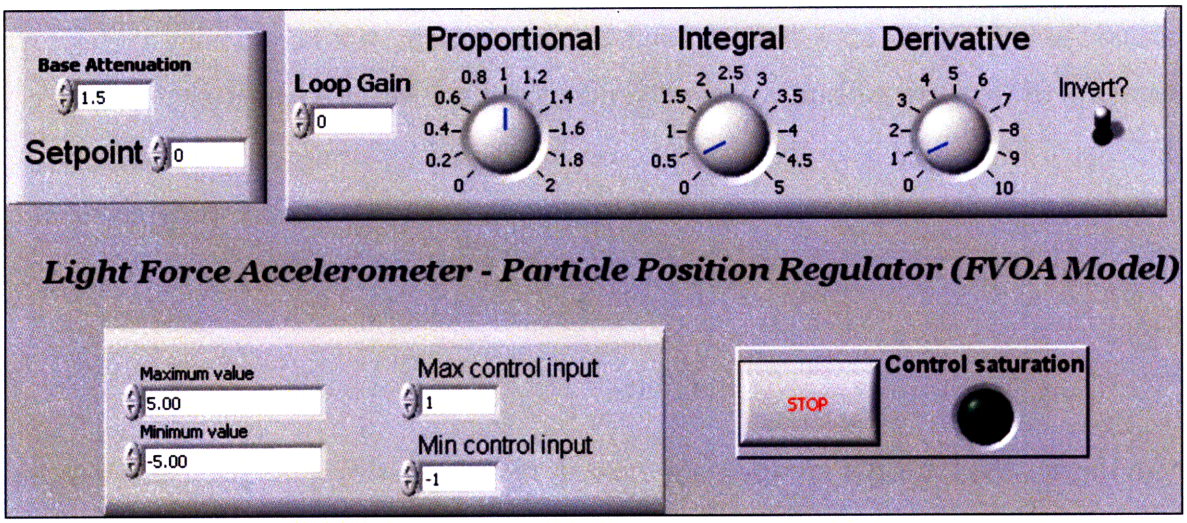

Figure B-1: Front panel of the particle position control program.

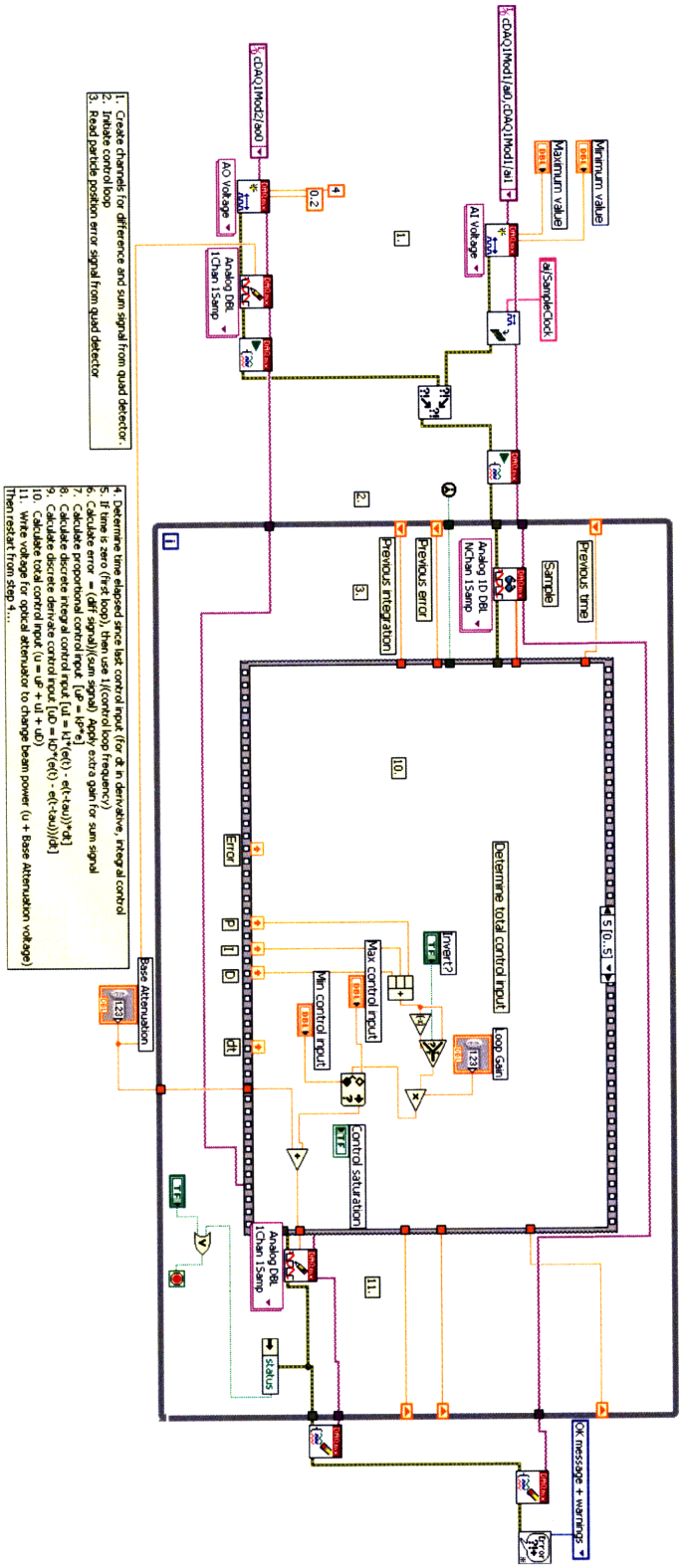

Figure B-2: Diagram of the particle position control program. Elements of the central stacked structure that are not shown simply calculate the proportional, integral, and derivate control components before being summed in the final frame.

THIS PAGE INTENTIONALLY LEFT BLANK

Bibliography

[AHV03] S. Arnold, M. Khoshsima, I. Teraoka, S. Holler, and F. Vollmer. "Shifts of whispering-gallery modes in microspheres by protein adsorption," *Optics Letters* **28**, 272, 2003.

[Arn82] S. Arnold and M. Lewittes. "Size dependence of the photophoretic force," *Journal of Applied Physics* **53**, 5314, 1982.

[Ash70] Arthur Ashkin. "Acceleration and Trapping of Particles by Radiation Pressure," *Physical Review Letters* **24**, 156, 1970.

[Ash71] A. Ashkin and J.M. Dziedzic. "Optical levitation by radiation pressure," *Applied Physics Letters* **19**, 8, 283, 1971.

[Ash74] A. Ashkin and J.M. Dziedzic. "Stability of optical levitation by radiation pressure," *Applied Physics Letters* **24**, 586, 1974.

[Ash76] A. Ashkin and J.M. Dziedzic. "Optical levitation in high vacuum," *Applied Physics Letters* **28**, 333, 1976.

[Ash77] A. Ashkin and J.M. Dziedzic. "Feedback stabilization of optically levitated particles," *Applied Physics Letters* **30**, 202, 1977.

[Ash83] A. Ashkin and J.P. Gordon. "Stability of radiation-pressure particle traps: an optical Earnshaw theorem." *Optics Letters* **8**, 511, 1983.

[Ash92] Arthur Ashkin. "Forces of a single-beam gradient laser trap on a dielectric sphere in the ray optics regime," *Biophysical Journal* **61**, 569, 1992.

[Ash97] Arthur Ashkin. "Optical trapping and manipulation of neutral particles using lasers," *Proceedings of the National Academy of Sciences* **94**, 4753, 1997.

[Ash07] Arthur Ashkin. Private commmunication, 2007.

[Bar01] Neil Barbour. "Inertial Components - Past, Present, and Future," *AIAA Guidance, Navigation and Control Conference*, 4290, August 2001.

[BaS01] N. Barbour and G. Schmidt. "Inertial Sensor Technology Trends," *IEEE Sensors Journal* **1**, 4, 332, 2001.

[BAS88] J.P. Barton, D.R. Alexander, and S.A. Schaub. "Internal and near-surface electromagnetic fields for a spherical particle irradiated by a focused laser beam," *Journal of Applied Physics* **64**, 1632, 1988.

[BAS89] J.P. Barton, D.R. Alexander, and S.A. Schaub. "Theoretical determination of net radiation force and torque for a spherical particle illuminated by a focused laser beam," *Journal of Applied Physics* **66**, 4594, 1989.

[Chu85] S. Chu, L. Hollberg, J.E. Bjorkholm, Alex Cable, and A. Ashkin. "Three-Dimensional Viscous Confinement and Cooling of Atoms by Resonance Radiation Pressure," *Physical Review Letters* **55**, 48, 1985.

[DaK95] K.B. Davis, M.O. Mewes, M.R. Andrews, N.J. van Druten, D.S. Durfee, D.M. Kurn, and W. Ketterle. "Bose-Einstein Condensation in a Gas of Sodium Atoms," *Physical Review Letters* **75**, 3969, 1995.

[Fin94] J.T. Finer, R.M. Simmons, and J.A. Spudich. "Single myosin molecule mechanics: piconewton forces and nanometre steps," *Nature (London)* **368**, 113, 1994.

[Fri96] M.E.J. Friese, J. Enger, H. Rubinsztein-Dunlop, and N.R. Heckenberg. "Optical angular-momentum transfer to trapped absorbing particles," *Physical Review A* **54** 54, 1996.

[Kas89] M. Kasevich, E. Riis, Steven Chu, and R.G. DeVoe. "rf spectroscopy in an atomic fountain," *Physical Review Letters* **63**, 612, 1989.

[Kel05] William Kelleher, Stephen P. Smith, and Richard E. Stoner. *Optically rebalanced accelerometer.* U.S. Patent 6,867,411, filed October 25, 2001, and issued March 15, 2005.

[Lai01] J.P. Laine, C. Tapalian, B. Little, and H. Haus. "Acceleration sensor based on high-Q optical microsphere resonator and pedestal antiresonant reflecting waveguide coupler," *Sensors and Actuators A* **93**, 1-7, 2001.

[Law98] Anthony Lawrence. *Modern Inertial Technology: Navigation, Guidance, and Control.* New York: Springer-Verlag, 1998.

[Mac90] Donald MacKenzie. *Inventing Accuracy.* Cambridge, MA: MIT Press, 1990.

[NST08] "Analysis of Time Domain Data," *Properties of Oscillator Signals and Measurement Methods*, NIST Time and Frequency Division, http://tf.nist.gov/phase/Properties/four.htm, 2008.

[PeC01] A. Peters, K.Y. Chung, and Steven Chu. "High-precision gravity measurements using atom interferometry," *Metrologia* **38**, 25, 2001.

[Plu85] A.B. Pluchino and S. Arnold. "Comprehensive model of the photophoretic force on a spherical microparticle," *Optics Letters* **10**, 261, 1985.

[RaP87] E.L. Raab, M. Prentiss, Alex Cable, Steven Chu, and D.E. Pritchard. "Trapping of Neutral Sodium Atoms with Radiation Pressure," *Physical Review Letters* **59**, 2631, 1987.

[Ree77] Larry D. Reed. "Low Knudsen number photophoresis," *Journal of Aerosol Science* **8**, 123, 1977.

[Sag13] G. Sagnac. "L'ether lumineux demontre par l'effet du vent relatif d'ether dans un interferometre en rotation uniforme," *Comptes Rendus de l'Academie des Science* **157**, 708, 1913.

[Sto05] Richard Stoner. Private communication, 2008.

[TiW04] D.H. Titterton and J.L. Weston. *Strapdown Inertial Navigation Technology.* Reston, VA: AIAA, 2004.

[Tve80] A.B. Tveten, A. Dandridge, C.M. Davis, and T.G. Giallorenzi. "Fibre optic accelerometer," *Electronics Letters (IEEE)* **16**, 854, 1980.

[VDH81] H.C. van de Hulst. *Light Scattering by Small Particles.* New York: Dover Publications, Inc., 1981.

[Ver98] D.W. Vernooy, V.S. Ilchenko, H. Mabuchi, E.W. Streed, and H.J. Kimble. 'High-Q measurements of fused-silica microspheres in the near infrared," *Optics Letters* **23**, 247, 1998.

[WuK05] G. Wurm and O. Krauss. "Photophoresis and the pile-up of dust in young circumstellar disks," *Astrophysical Journal* **630**, 1088, 2005.

[Yal76] Yu. I. Yalamov, V.B. Kutukov, and E.R. Shchukin. "Theory of the photophoretic motion of the large-size volatile aerosol particle," *Journal of Colloid Interface Science* **57**, 564, 1976.